
Physics-Informed Generative Modeling of Wireless Channels

Benedikt Böck¹ Andreas Oeldemann² Timo Mayer² Francesco Rossetto² Wolfgang Utschick¹

Abstract

Learning the distribution of the wireless channel within a specific environment of interest is essential to exploit the full potential of machine learning (ML) for wireless communications and radar applications. Generative modeling offers a promising framework to address this problem. However, existing approaches pose unresolved challenges, including the need for high-quality training data, limited generalizability, and a lack of physical interpretability. To address these issues, we propose a model that combines the physics-related compressibility of wireless channels with sparse Bayesian generative modeling (SBGM) to learn the distribution of the underlying physical channel parameters. By leveraging the sparsity-inducing characteristics of SBGM, our method can learn from compressed observations received by an access point (AP) during default online operation. Moreover, it is physically interpretable and generalizes to arbitrary system configurations without requiring retraining.

1. Introduction

Accurate wireless channel modeling is critical for system design, network optimization and performance evaluation in wireless communications and radar applications (Wang et al., 2018; 2020; Yin & Cheng, 2016). Generally, there are two different approaches to wireless channel modeling: physically and analytically oriented (Almers et al., 2007). The former integrates the underlying physics in the description of wireless channels and focuses on the model’s accuracy and realism. In contrast, the latter captures the channel statistics ignoring the underlying physics and provides an easy-to-use framework that facilitates the embedding in evaluation and system design schemes (Almers et al., 2007; Imoize et al., 2021). Standardized channel models such as the 3GPP (3GPP, 2024a), COST (Liu et al., 2012) or WINNER (Meinilä et al., 2009) families are physically oriented and combine physics with stochastic properties of wireless

channels. Specifically, by using the laws of electromagnetic wave propagation, these channel models deterministically describe the wireless channel as a function of the corresponding physical parameters (directions of arrival (DoAs), delays, etc.), which in turn are characterized statistically. These statistical properties are calibrated and evaluated by real-world measurement campaigns in different types of propagation environments such as indoor, outdoor, urban, and rural (Yin & Cheng, 2016). While these models characterize the wireless channel in various generic scenarios and are widely accepted in the communications community, they also come with some considerable drawbacks.

Due to their broad categorization of channels into generic scenario types, such as indoor and outdoor, these channel models cannot represent the unique characteristics of one specific environment of interest and, thus, cannot be used to adapt networks to their scenario. This limits their application to ML-aided wireless communications, where ML models are supposed to be trained on scenario-specific channel realizations (Kim et al., 2023). Moreover, there is an emerging variety of different wireless communications settings such as millimeter wave (mmWave), unmanned aerial vehicles (UAV), high-speed train (HST), ultra-massive multiple-input-multiple-output (MIMO), and Internet of things (IoT) communications, each with its own unique requirements for accurate channel modeling, imposing new and open challenges on the measurement campaigns and channel sounders (Wang et al., 2020). Additionally, as these models have evolved, they have become increasingly accurate by incorporating more physical effects. However, this improved accuracy comes at the cost of simplicity, making it more challenging to integrate these models directly into real-time processing tasks, and resulting in an undesired trade-off between accuracy and simplicity (Imoize et al., 2021).

One physically oriented alternative is ray tracing, which models the channel purely deterministically. Ray tracing is a technique for simulating the propagation of electromagnetic waves in specific scenarios dating back to the 16th century (Hofmann, 1990). Using ray tracing for modeling wireless channels requires a 3D digital replica of the environment of interest and an accurate characterization of the materials within the scene (Geok et al., 2018; McKown & Hamilton, 1991; Yun & Iskander, 2015). Commercial ray tracing tools like WirelessInside (Remcom) use databases to

¹Technical University of Munich, Munich, Germany
²Rohde&Schwarz, Munich, Germany. Correspondence to: Benedikt Böck <benedikt.boeck@tum.de>.

determine the material properties within the scene, requiring full environmental knowledge. To address this limitation, differentiable ray tracing is studied in (Gan et al., 2014; Hoydis et al., 2024; Orekondy et al., 2023), enabling the learning of material properties from data. On the downside, high-quality channel state information (CSI) must be collected for training in each scenario of interest, questioning its practicality. Additionally, the accurate modeling of diffuse scattering and the computational complexity remain challenging objectives in ray tracing (Imoize et al., 2021).

Another approach for channel modeling is based on generative modeling, which aims to learn an unknown distribution from data (Bond-Taylor et al., 2022). Using the terminology from (Diggle & Gratton, 1984), generative models can be categorized into *prescribed* and *implicit* models. *Prescribed* models learn a parameterized statistical model of the distribution of interest (Girin et al., 2021). In contrast, *implicit* models directly learn the stochastic procedure to generate samples (Mohamed & Lakshminarayanan, 2017). Examples of the former are variational autoencoders (VAEs) (Kingma & Welling, 2014), while generative adversarial networks (GANs) (Goodfellow et al., 2014) represent the latter. Perhaps surprisingly, almost all approaches to modeling wireless channels with generative models in the current literature use GANs and are, thus, relying on *implicit* modeling (Euchner et al., 2024; Hu et al., 2023; Li et al., 2018; Orekondy et al., 2022; Seyedsalehi et al., 2019; Tian et al., 2024; Xiao et al., 2022; Yang et al., 2019). Moreover, since this line of research applies GANs in a black box manner and does not incorporate underlying physics, these methods belong to the class of analytically oriented channel models. While these publications show some progress in channel modeling with *implicit* generative models, there are several open concerns with this approach (Euchner et al., 2024):

High-quality datasets: The assumption of having access to (lots of) scenario-specific high-quality training data requires costly measurement campaigns in each scenario of interest.

Generalizability: The proposed GAN-based methods only generate channel realizations matching the system configuration (number of antennas, subcarrier spacing etc.) used for training, making it difficult to adapt to other configurations.

Physical interpretability & consistency: Their generation process cannot be interpreted physically and they cannot guarantee their samples to obey the underlying physics.

In this work, we demonstrate how *prescribed* generative models can effectively resolve all these limitations. More specifically, we show that the parameterized statistical models in *prescribed* generative modeling enable the integration of the underlying physics of electromagnetic wave propagation. This adaption not only relaxes the requirements for the training data but also shifts the generative modeling

approach from the analytically oriented to the physically oriented channel models and provides generalizability, interpretability, and physical consistency. Our approach shares features with standardized channel models, as it also describes the wireless channel as a deterministic function of the physical parameters. In contrast, however, the statistical model that characterizes these parameters does not need to be calibrated through extensive and costly measurement campaigns but can be trained by a few compressed and noisy channel observations that an AP or a base station (BS) receives during default online operation. Our method aligns with the idea of physics-informed ML, i.e., facilitating the learning process from training data by incorporating underlying pre-known physics that the trained model must obey (Karniadakis et al., 2021; Raissi et al., 2019). However, instead of integrating partial differential equations from physics into a loss function, we leverage the laws of ray optics, which build upon the physics of electromagnetic wave propagation and relate the wireless channel to its underlying physical parameters (e.g., delays and angles).

Main Contributions We combine the physics-related compressibility of wireless channels with SBGM and knowledge about conditional channel models to develop a *prescribed* physics-informed generative model for wireless channels. In particular, our model resolves the limitations of existing approaches, i.e., it does not need high-quality training data, it generalizes to arbitrary system configurations without requiring retraining, and it is physically consistent and interpretable. Moreover, we derive novel closed-form solutions for the M-step of one Gaussian mixture model (GMM)-based variant of our proposed method that builds on a Kronecker factorization of the learned covariances. Eventually, we validate the performance on several datasets of wireless channels, showing the superiority of our approach for physical channel parameter generation and generating channel realizations.

2. Related Work

Early work exploiting *implicit* GAN-based generative models for wireless channel modeling is given by (Li et al., 2018; Yang et al., 2019). Since then, several GAN variants have been investigated for modeling either time-varying (Seyedsalehi et al., 2019) or MIMO channel impulse responses (Orekondy et al., 2022; Xiao et al., 2022). For evaluation, (Orekondy et al., 2022; Seyedsalehi et al., 2019; Xiao et al., 2022) use cluster delay line, tap delay line or extended pedestrian A-like 3GPP channel models (3GPP, 2023; 2024a). These link-level models produce training channels that all originate from the same set of cluster angles and delays. Thus, they cannot accurately represent entire communications environments where users experience different sets of delays, DoAs and directions of departure (DoDs). The

work in (Euchner et al., 2024; Hu et al., 2023) also exploits GANs to learn MIMO channel impulse responses and leverages the geometry-based stochastic channel model (GSCM) QuaDRiGa (Jaeckel et al., 2014) or measurement data for evaluation. Diffusion models (DMs) for learning MIMO channels has been considered in (Lee et al., 2024; Sengupta et al., 2023). Learning to generate physical channel parameter realizations, such as delays and DoAs, has been investigated for UAV communications with GANs and VAEs in (Tian et al., 2024; Xia et al., 2022). Both assume a large ground-truth dataset of physical channel parameters to be accessible and utilize ray tracing for evaluation. In (Baur et al., 2024b; Fesl et al., 2023), GMMs and VAEs are used for channel estimation. While they do not consider physical parameters, they also train on compressed observations. Moreover, (Baur et al., 2024c) introduces wireless communications-specific evaluation techniques to evaluate generative models trained to generate channel realizations.

3. Background and Problem Statement

3.1. Physically Characterizing Wireless Channels

Wireless signal transmission causes the signal to attenuate and undergo phase shifts. Moreover, as the signal propagates, it can also get reflected or scattered by obstacles in the environment. This results in multiple paths (or rays) between the transmitter and receiver, each characterized by its own attenuation and phase shift, which, in turn, are linked to the physical channel parameters (e.g., angles and delays) through geometrical optics. The wireless signal transmission can be modeled as a linear time-variant system (Tse & Viswanath, 2005) and, thus, these effects are captured by the corresponding wireless baseband channel (transfer function), which depends on the time t , the (baseband) frequency f , and the receiver and transmitter positions \mathbf{r}_R and \mathbf{r}_T in local coordinate systems, i.e.,

$$h(t, f, \mathbf{r}_R, \mathbf{r}_T) = \sum_{\ell=1}^L \sum_{m=1}^{M_\ell} \rho_{\ell,m} e^{-j2\pi\vartheta_{\ell,m}t} e^{-j2\pi\tau_{\ell,m}f} \times e^{-j\mathbf{k}(\boldsymbol{\Omega}_{\ell,m}^{(R)})^T \mathbf{r}_R} e^{-j\mathbf{k}(\boldsymbol{\Omega}_{\ell,m}^{(T)})^T \mathbf{r}_T}. \quad (1)$$

The corresponding physical channel parameters contain the number L of paths, the number M_ℓ of subpaths per path ℓ , the complex path losses $\rho_{\ell,m}$, the doppler shifts $\vartheta_{\ell,m}$, the delays $\tau_{\ell,m}$, the DoAs $\boldsymbol{\Omega}_{\ell,m}^{(R)}$, and the DoDs $\boldsymbol{\Omega}_{\ell,m}^{(T)}$. The wavevector $\mathbf{k}(\cdot)$ is defined as $\mathbf{k}(\cdot) = (2\pi/\lambda) \mathbf{e}(\cdot)$ with wavelength λ and $\mathbf{e}(\cdot)$ is the unit vector in spherical coordinates. Transforming (1) via a Fourier transform (FT) with respect to any of its arguments results in their dual so-called dispersive domains (Yin & Cheng, 2016). Moreover, one is typically interested in a sampled version of the wireless channel $h(\cdot)$. For instance, when the receiver and transmitter are equipped with multiple antennas, the process of

receiving and transmitting signals by their antenna arrays can be viewed as sampling the wireless channel $h(\cdot)$ in (1) at the antennas' spatial positions. By exemplarily taking the FT in the frequency domain, ignoring the channel's temporal evolution (i.e., $t = 0$) and accounting for the spatial sampling via multiple antennas, (1) can be represented as

$$\mathbf{H}(\tau) = \sum_{\ell=1}^L \sum_{m=1}^{M_\ell} \rho_{\ell,m} \delta(\tau - \tau_{\ell,m}) \mathbf{a}_R(\boldsymbol{\Omega}_{\ell,m}^{(R)}) \mathbf{a}_T(\boldsymbol{\Omega}_{\ell,m}^{(T)})^T \quad (2)$$

with $\mathbf{a}_R(\cdot)|_i = e^{-j\mathbf{k}(\cdot)^T \mathbf{r}_{R,i}}$, $\mathbf{a}_T(\cdot)|_j = e^{-j\mathbf{k}(\cdot)^T \mathbf{r}_{T,j}}$ and $\mathbf{r}_{R,i}$ and $\mathbf{r}_{T,j}$ being the positions of the i th and j th antenna of the receiver and transmitter, respectively.¹ Equation (2) represents the generic MIMO channel impulse response, which does not cover the temporal domain. As another example, the receiver and transmitter in orthogonal-frequency-division-multiplexing (OFDM) are both equipped with single antennas, whose positions can be set to the coordinate systems' origins, i.e., $\mathbf{r}_{T/R,1} = \mathbf{0}$. Thus, OFDM covers no spatial domains and is characterized by its subcarrier spacing Δf and symbol duration ΔT . This setup corresponds to equidistantly sampling (1) in both the frequency and temporal domains, yielding the OFDM channel matrix

$$\mathbf{H} = \sum_{\ell=1}^L \sum_{m=1}^{M_\ell} \rho_{\ell,m} \mathbf{a}_t(\vartheta_{\ell,m}) \mathbf{a}_f(\tau_{\ell,m})^T \quad (3)$$

with $\mathbf{a}_t(\vartheta_{\ell,m})|_i = e^{-j2\pi\vartheta_{\ell,m}(i-1)\Delta T}$ and $\mathbf{a}_f(\tau_{\ell,m})|_j = e^{-j2\pi\tau_{\ell,m}(j-1)\Delta f}$. For our following considerations, we define the set of physical channel parameters

$$\mathcal{P} = \{\rho_{\ell,m}, \vartheta_{\ell,m}, \tau_{\ell,m}, \boldsymbol{\Omega}_{\ell,m}^{(R)}, \boldsymbol{\Omega}_{\ell,m}^{(T)}\}_{\ell,m=1}^{L,M_\ell}. \quad (4)$$

We specify subsets containing the parameters associated with a specific domain by their subscript, e.g., $\mathcal{P}_R = \{\rho_{\ell,m}, \boldsymbol{\Omega}_{\ell,m}^{(R)}\}_{\ell,m=1}^{L,M_\ell}$ or $\mathcal{P}_{t,f} = \{\rho_{\ell,m}, \vartheta_{\ell,m}, \tau_{\ell,m}\}_{\ell,m=1}^{L,M_\ell}$.

3.2. System Models and Problem Statement

We consider a scenario in which an AP receives channel observations \mathbf{y}_i from different locations within the environment it serves. One example is outdoor communications, where users periodically send pilot symbols to their BS. The observations are noisy and potentially compressed, i.e.,

$$\mathbf{y} = \mathbf{A}\mathbf{h} + \mathbf{n} \quad (5)$$

where \mathbf{h} represents the channel, \mathbf{A} is the measurement matrix, and \mathbf{n} is additive white Gaussian noise (AWGN). The AP eventually collects a training dataset $\mathcal{Y} = \{\mathbf{y}_i\}_{i=1}^{N_t}$ that captures information from the entire environment. We particularly focus on the following two scenarios in our work.

¹Although λ technically depends on f and should be considered in the FT in (2), it can be well approximated as constant when the considered bandwidth is much smaller than the center frequency.

Narrowband static single-input-multiple-output (SIMO): The receiver is equipped with multiple antennas, whereas the transmitter has a single antenna. The channel \mathbf{h} only covers the spatial receiver domain, i.e., \mathbf{h} is given by (2) with $\mathbf{a}_T(\cdot) = \mathbf{1}$ and no τ -dependency. The observation matrix \mathbf{A} in (5) equals the identity, i.e., $\mathbf{A} = \mathbf{I}_{M_R}$.

Double-selective OFDM: The channel \mathbf{h} in (5) covers no spatial domain, and vectorizes (3), i.e., $\mathbf{h} = \text{vec}(\mathbf{H})$. The observation matrix \mathbf{A} is a selection matrix, i.e., its rows are distinct unit vectors, masking out particular entries of \mathbf{h} .

As the channel \mathbf{h} does not cover all four possible domains in these systems, only a subset of \mathcal{P} in (4) determines \mathbf{h} . Thus, depending on the employed system, the environment is characterized by a distribution over this subset of physical parameters, i.e., $p(\mathcal{P}_R)$ in SIMO and $p(\mathcal{P}_{t,f})$ in OFDM. This work aims to develop a physics-informed generative model that can learn these distributions solely using the imperfect training dataset \mathcal{Y} . While this work focuses on SIMO and OFDM, there is a straightforward generalization to other systems, such as MIMO and MIMO-OFDM.

4. Proposed Method

4.1. Channel Sparsity

In a first step towards a physics-informed generative model, we utilize the property of wireless channels to be compressible (i.e., approximately sparse) with respect to a physically interpretable dictionary, which has been used for channel and parameter estimation (Dai & So, 2021; Gaudio et al., 2022). For instance, by considering the SIMO channel in Section 3.2, placing the antennas with $\lambda/2$ spacing in a uniform linear array (ULA), aligning the local coordinate system's z-axis with the ULA, and assuming the far-field approximation to hold, the DoAs $\Omega_{\ell,m}^{(R)}$ reduce to single position-independent angles $\omega_{\ell,m}^{(R)} \in [-\pi/2, \pi/2)$ with $\mathbf{a}_R(\cdot)|_i = e^{-j\pi(i-1)\sin(\cdot)}$ in (2). By defining a grid $\mathcal{G}_R = \{g\pi/S_R\}_{g=-S_R/2}^{S_R/2-1}$ with S_R being the number of grid-points, one can represent the SIMO channel by

$$\mathbf{h} = \sum_{g=-S_R/2}^{S_R/2-1} s_R^{(g)} \mathbf{a}_R\left(\frac{g\pi}{S_R}\right) = \mathbf{D}_R \mathbf{s}_R \quad (6)$$

with $\mathbf{D}_R = [\mathbf{a}_R(-\frac{\pi}{2}), \dots, \mathbf{a}_R(\frac{\pi}{2} - \frac{\pi}{S_R})]$ and $\mathbf{s}_R = [s_R^{(-S_R/2)}, \dots, s_R^{(S_R/2-1)}]^\top$. Moreover, if the DoAs $\omega_{\ell,m}^{(R)}$ coincide with grid points in \mathcal{G}_R , the entries $s_R^{(g)}$ fulfill $s_R^{(g)} = \rho_{\ell,m}$ if $\omega_{\ell,m}^{(R)} = g\pi/S_R$ and are zero else. In this case, \mathbf{s}_R perfectly determines the channel's physical parameters \mathcal{P}_R . Since this usually only approximately holds, \mathbf{s}_R is typically not exactly sparse but rather compressible. Equivalent compressible representations also exist in the frequency and temporal domain. Specifically, by intro-

ducing the grid $\mathcal{G}_t \times \mathcal{G}_f$ with $\mathcal{G}_t = \{i\bar{\nu}/S_t\}_{i=-S_t/2}^{S_t/2-1}$ and $\mathcal{G}_f = \{j\bar{\tau}/S_f\}_{j=0}^{S_f-1}$, where $\bar{\nu}/2$ and $\bar{\tau}$ bound the maximally reachable doppler shift and delay, and $S_t, S_f \in \mathbb{N}$, we also find a compressible representation of the vectorized OFDM channel in (3) equivalent to (6), i.e., $\mathbf{h} = \mathbf{D}_{t,f} \mathbf{s}_{t,f}$ with $\mathbf{D}_{t,f} = \mathbf{D}_t \otimes \mathbf{D}_f$. A more detailed description is given in Appendix A.

In general, choosing a grid \mathcal{G}_R or $\mathcal{G}_t \times \mathcal{G}_f$ with sufficiently high resolution enables the vectors \mathbf{s}_R or $\mathbf{s}_{t,f}$ to uniquely determine the channel's physical parameters \mathcal{P}_R or $\mathcal{P}_{t,f}$. As a result, we replace the learning of $p(\mathcal{P}_R)$ and $p(\mathcal{P}_{t,f})$ by instead learning $p(\mathbf{s}_R)$ and $p(\mathbf{s}_{t,f})$, with the grid resolution being the hyperparameter that controls the approximation error. In particular, this replacement enables the integration of structural prior knowledge into the learning, since we know \mathbf{s}_R and $\mathbf{s}_{t,f}$ to be compressible. Moreover, this prior knowledge also allows us to integrate the notion of generative modeling, as the following section shows.

4.2. Sparse Bayesian Generative Modeling

Building on Section 4.1, we aim to learn $p(\mathbf{s}_R)$ (or $p(\mathbf{s}_{t,f})$) with \mathbf{s}_R and $\mathbf{s}_{t,f}$ being generally compressible. To do so, we build upon SBGM introduced in (Böck et al., 2024b). SBGM is a framework that enables the learning of a non-trivial parameterized distribution $p_{\theta,\delta}(s)$ for the compressible representation s of a signal or image x of interest with respect to some pre-known dictionary \mathbf{D} , i.e., $x = \mathbf{D}s$. A key feature of SBGM is that the learning can be done solely using training data of noisy and compressed measurements $\mathbf{y}_i = \mathbf{A}\mathbf{x}_i + \mathbf{n}_i$ with \mathbf{n}_i being AWGN. For that, SBGM combines sparse Bayesian learning (SBL) (Tipping, 2001; Wipf & Rao, 2004) with a specific class of *prescribed* generative models, namely, conditionally Gaussian latent models (CGLMs), i.e., models with a conditioned Gaussian on a latent variable z . After a minor extension to the complex-valued case, the statistical model in SBGM is given by

$$\mathbf{y}|\mathbf{s} \sim p(\mathbf{y}|\mathbf{s}) = \mathcal{N}_{\mathbb{C}}(\mathbf{y}; \mathbf{A}\mathbf{D}\mathbf{s}, \sigma^2 \mathbf{I}), \quad (7)$$

$$\mathbf{s}|\mathbf{z} \sim p_{\theta}(\mathbf{s}|\mathbf{z}) = \mathcal{N}_{\mathbb{C}}(\mathbf{s}; \mathbf{0}, \text{diag}(\gamma_{\theta}(\mathbf{z}))), \quad (8)$$

$$\mathbf{z} \sim p_{\delta}(\mathbf{z}) \quad (9)$$

with pre-known measurement matrix \mathbf{A} , learnable parameters θ and δ , variance σ^2 modeling the noise in the measurement, further latent variable z , and \mathbf{s} follows a conditionally zero-mean Gaussian $p_{\theta}(\mathbf{s}|\mathbf{z})$ with z -dependent diagonal covariance matrix. The work in (Böck et al., 2024b) shows that this particular choice of $p_{\theta}(\mathbf{s}|\mathbf{z})$ serves as a sparsity promoting regularization. After training, $p_{\delta,\theta}(s)$ is used for regularizing linear inverse problems and has been demonstrated to outperform standard priors in compressive sensing (Böck et al., 2024b). By choosing \mathbf{D} in (7) to be \mathbf{D}_R (or $\mathbf{D}_{t,f}$) in Section 4.1, we can apply the training from SBGM and learn the parameterized distribution for \mathbf{s}_R (or $\mathbf{s}_{t,f}$) and,

thus, for the physical channel parameters using solely noisy and compressed channel observations. However, a main drawback of SBGM is that s exhibits a universal conditional zero mean, i.e., $\mathbb{E}[s|z] = \mathbf{0}$ for all z (cf. (8)). Following the discussion in (Böck et al., 2024b), this strictly limits its capability of generating realistic samples as it is typically not possible to decompose the true unknown distribution $p(s)$ in this way.

Remarkably, wireless channels exhibit a unique property that provably eliminates this limitation in its entirety when incorporating the common assumption of stationarity. Thus, SBGM is particularly well suited for modeling and generating wireless channels, as the following section shows.

4.3. Structured Conditional Channel Moments

Generally, the complex path loss phases $\arg(\rho_{\ell,m})$ in (1) are modeled to be uniformly distributed (Tse & Viswanath, 2005) rendering the wireless channel to have a zero mean. Moreover, by assuming \mathcal{P} in (4) to not depend on the frequency, time, or antenna positions, the channel (1) is a wide sense stationary (WSS) process in any domain and exhibits Toeplitz structured covariance matrices when being uniformly sampled (Böck et al., 2024a), as it is the case in SIMO and OFDM. When we assign (8) to the compressible representation of the channel in, e.g., (6), we see that (8) enforces the channel \mathbf{h} to exhibit a universal conditional zero mean, i.e., $\mathbb{E}[\mathbf{h}|z] = \mathbf{0}$ for all z and a conditional covariance matrix $\mathbb{E}[\mathbf{h}\mathbf{h}^H|z]$ representable by $\mathbf{D}_R \text{diag}(\gamma_\theta(z)) \mathbf{D}_R^H$. Latter is Toeplitz (or block-Toeplitz) when using \mathbf{D}_R (or $\mathbf{D}_{t,f} = \mathbf{D}_t \otimes \mathbf{D}_f$) from Section 4.1. We utilize insights from (Böck et al., 2024a) to show that these structural constraints, i.e., the conditional zero mean and Toeplitz covariance matrix, precisely align with CGLMs when being properly trained on wireless channels.² Specifically, (Böck et al., 2024a) shows that if a variable does not contain information about the path loss phases $\arg(\rho_{\ell,m})$, the conditioning on this variable preserves the channel’s zero mean and Toeplitz covariance structure. By observing that the phases $\arg(\rho_{\ell,m})$ cannot represent environment-specific channel features, (Böck et al., 2024a) reasons that the latent variable z of CGLMs does not contain $\arg(\rho_{\ell,m})$ -related information as the training of CGLMs aims to capture characteristic statistical features by their latent variable z . Thus, the conditioning on z preserves the channel’s zero mean and Toeplitz covariance structure, and the structural constraints (i.e., the zero mean and diagonal covariance) enforced in (8) align with the characteristics of the true, unknown $p(s)$ for wireless channels. Thus, the generation-concerning limitation in (Böck et al., 2024b) for SBGM does not apply for wireless channels, and (8) and (9) can perfectly capture the true $p(s)$ by using the dictionaries in Section 4.1.

²We refer to Appendix B for a more detailed explanation.

4.4. Compressive Sensing GMMs and VAEs

Sections 4.1-4.3 provide the means to understand why SBGM (7)-(9) can learn the distribution of the physical channel parameters based on a training set of noisy and compressed channel observations. Generally, (Böck et al., 2024b) introduces a VAE and a GMM variant, the compressive sensing VAE (CSVAE) and compressive sensing GMM (CSGMM), as particular implementations of the statistical model (7)-(9). Since the CSGMM and CSVAE closely resemble the models in our work, we summarize their setup, highlight mild differences to (Böck et al., 2024b), provide detailed information in Appendices C-E, but keep their acronyms for the proposed models in this work.³

Dataset Our dataset assumptions differ from those in (Böck et al., 2024b) which assumes the noise variance to stay constant. However, considering varying noise variances σ_i^2 for wireless channels is more realistic since users further away from their AP experience a smaller signal-to-noise ratio (SNR).⁴ Thus, we consider the training set

$$\mathcal{Y} = \{\mathbf{y}_i | \mathbf{y}_i = \mathbf{A}\mathbf{h}_i + \mathbf{n}_i\}_{i=1}^{N_t}; \mathbf{n}_i \sim \mathcal{N}(\mathbf{0}, \sigma_i^2 \mathbf{I}). \quad (10)$$

CSVAE Motivated by VAEs, we choose $p_\delta(z) = \mathcal{N}(z; \mathbf{0}, \mathbf{I})$. The parameterization θ of $\gamma_\theta(z)$ is realized by a neural network (NN). Equivalent to VAEs, the log-evidence for CSVAEs is intractable, which is why a variational Gaussian $q_\phi(z|\mathbf{y}) = \mathcal{N}(z; \boldsymbol{\mu}_\phi(\mathbf{y}), \text{diag}(\boldsymbol{\sigma}_\phi^2(\mathbf{y})))$ is integrated, whose parameters ϕ are also realized by a NN. For training, (Böck et al., 2024b) derives an extended evidence lower bound (ELBO) $L(\theta, \phi)$ taking into account the additional latent variable s in (7)-(9). The objective that is maximized for training approximates $L(\theta, \phi)$ with a single-sample Monte-carlo estimation and equals

$$\sum_{\mathbf{y}_i \in \mathcal{Y}} \left(\mathbb{E}_{p_\theta(s|\tilde{z}_i, \mathbf{y}_i)} [\log p(\mathbf{y}_i|s)] - \text{D}_{\text{KL}}(q_\phi(z|\mathbf{y}_i)||p(z)) - \text{D}_{\text{KL}}(p_\theta(s|\tilde{z}_i, \mathbf{y}_i)||p_\theta(s|\tilde{z}_i)) \right) \quad (11)$$

with $\tilde{z}_i \sim q_\phi(z|\mathbf{y}_i)$. A key aspect in SBGM is that $p_\theta(s|\tilde{z}_i, \mathbf{y}_i)$ is a Gaussian with closed-form mean and covariance specified in Appendix C. Based on these, all terms in (11) can be calculated and are given in Appendix D.

CSGMM Motivated by GMMs, we choose $p_\delta(z)$ to be a categorical distribution, i.e., $p_\delta(z) = p_\delta(k) = \rho_k$ ($k = 1, \dots, K$). Moreover, $\gamma_\theta(z) = \gamma_k$, i.e., s follows a GMM with zero means and diagonal covariance matrices. The

³For a very detailed overview, we refer to (Böck et al., 2024b).

⁴While the actual noise variance mainly depends on the receiver hardware and, thus, does not vary between users at different locations, the typical channel-wise pre-processing of normalizing by an estimated path loss effectively results in varying noise variances.

learning of $\{\rho_k, \gamma_k\}_{k=1}^K$ is done by an extended expectation-maximization (EM) algorithm considering the additional latent variable s in (7)-(9) (Böck et al., 2024b). In the E-step, the model’s posterior $p(s, k | \mathbf{y}_i) = p(s | k, \mathbf{y}_i) p(k | \mathbf{y}_i)$ has to be computed for each training sample \mathbf{y}_i . Equivalent to the CSVAE, $p(s | k, \mathbf{y}_i)$ is Gaussian with closed-form mean and covariance (cf. Appendix C) also resulting in a closed-form E-step. The M-step equals the one in (Böck et al., 2024b). Both are summarized in Appendix E.

Kronecker Approximation In case of considering multiple domains (e.g., the time and frequency domain in OFDM, cf. Section 3.2), one possibility to reduce the number of learnable parameters is to constrain the conditional covariance matrix $\mathbb{E}[\mathbf{h}\mathbf{h}^H | \mathbf{z}]$ to not only be block-Toeplitz (cf. Section 4.3) but rather a Kronecker of Toeplitz matrices forming a subset of all block-Toeplitz matrices. In particular, by constraining $\gamma_\theta(\mathbf{z}) = \gamma_\theta^{(t)}(\mathbf{z}) \otimes \gamma_\theta^{(f)}(\mathbf{z})$ the resulting conditional channel covariance matrix $\mathbf{D}_{t,f} \text{diag}(\gamma_\theta(\mathbf{z})) \mathbf{D}_{t,f}^H$ in OFDM is given by

$$(\mathbf{D}_t \otimes \mathbf{D}_f) \text{diag}(\gamma_\theta^{(t)}(\mathbf{z}) \otimes \gamma_\theta^{(f)}(\mathbf{z})) (\mathbf{D}_t \otimes \mathbf{D}_f)^H \quad (12)$$

and, thus, can be written as a Kronecker product of Toeplitz covariance matrices. This approximation reduces the number of variance parameters learned from $S_t S_f$ to $S_t + S_f$. For the CSVAE, this constraint can be enforced by letting the NN output an S_f - and an S_t -dimensional vector and subsequently building the Kronecker product instead of outputting a $S_f S_t$ -dimensional vector. For CSGMM, incorporating this constraint requires a new M-step. Specifically, the M-step with the constraint $\gamma_k = \gamma_k^{(t)} \otimes \gamma_k^{(f)}$ exhibits no closed form and must be solved iteratively. We derive a closed form for the global solution of the update steps when applying coordinate search in Appendix F.

Moreover, we provide pseudocode for generating channel parameters as well as channel realizations in Appendix M.

5. Discussion

Generalizability Section 4 addresses how our proposed method circumvents the need for high-quality training data and provides physical interpretability and consistency. One more remaining claim from Section 1 is generalizability, i.e., the adaptability to other system configurations, such as different numbers of antennas or subcarrier spacings after training. While the range of the dictionaries in Section 4.1 depends on the system configuration (e.g., the number of antennas determines the dimension of the range of \mathbf{D}_R), the dictionary’s domain only depends on the chosen grid (e.g., \mathcal{G}_R) and, thus, is configuration-independent. Moreover, the learned statistical model (8) and (9) does not depend on the dictionary used for training. In consequence, when sampling

a new s from (8) and (9) after training and computing the corresponding channel realization \mathbf{h} , we can use a new dictionary $\mathbf{D}^{(\text{new})}$, whose domain must match the dictionary used for training, but whose range can be easily adapted to a newly desired system configuration without any retraining.

Providing Training Data for Wireless Communications

Most ML-based methods for the physical layer in wireless communications either require lots of ground-truth and scenario-specific channel realizations for training or at least scenario-specific pairs of input and output signals linked by the wireless channels. However, finding efficient and scalable ways to obtain this data in each scenario of interest is an open challenge (Kim et al., 2023). With our proposed method, we present a solution to this problem. Our method can learn from corrupted data that a wireless receiver obtains, e.g., during default online operation. It then can generate a desired amount of scenario-specific clean channel realizations for, e.g., training other ML-based methods.

Foundation Modeling Perspective

While our method can generate training data, it can also be directly used for real-time processing tasks. Recently, VAEs and GMMs have been used for channel estimation (Baur et al., 2024a; Böck et al., 2023; Fesl et al., 2024; Koller et al., 2022), channel prediction (Turan et al., 2024a), and precoder- and pilot design (Turan et al., 2024b; 2025). Thus, the CSVAE and CSGMM not only generalize to arbitrary system configurations but also provide information that can be directly used for these downstream tasks without the need for specific training. This aligns with the idea of foundation modeling, i.e., training a generalized ML model and applying it to various downstream tasks without retraining.

Limitations Our method has limitations related to non-stationary channel generation, off-grid mismatches, and OFDM pilot patterns, which are discussed in Appendix G.

6. Experiments

6.1. Experimental Setup

Datasets We evaluate our method’s performance on three datasets. First, we use a modified standardized 3GPP spatial channel model for SIMO, which we adapted to better illustrate our method. Second, for simulations with OFDM, we use QuaDRiGa (Jaekel et al., 2014). Finally, we also use the ray tracing database DeepMIMO (Alkhateeb, 2019) for a further evaluation on SIMO in Appendix L. For the channel observations in OFDM, we generate one random selection matrix \mathbf{A} extracting M entries from \mathbf{h} and apply it to every training channel (cf. (10)). In any simulation, we draw a SNR uniformly distributed between 0 and 20dB for each training sample individually, which we use to com-

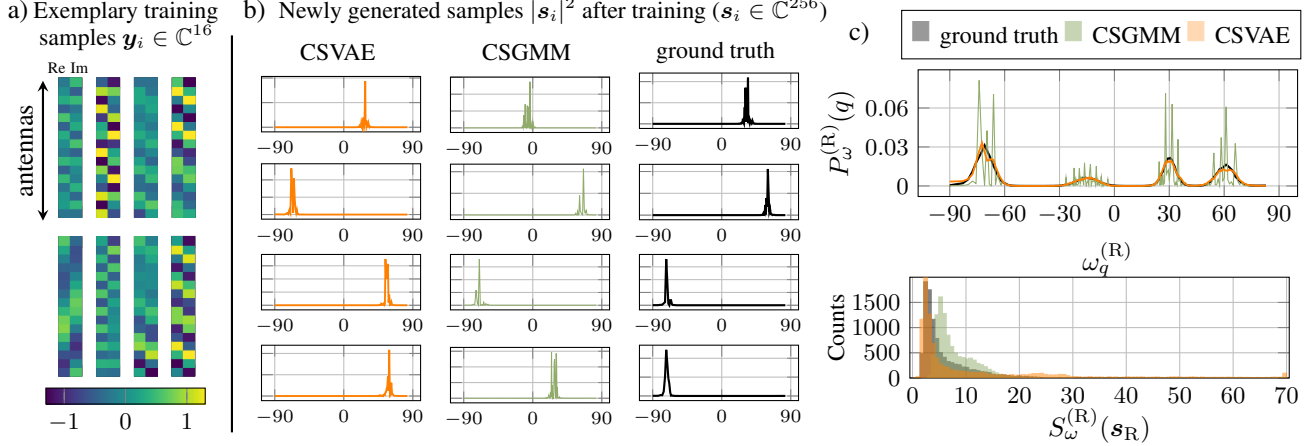


Figure 1. a) Eight exemplary training samples, b) squared absolute value of four exemplary generated samples of CSVAE, CSGMM and ground truth, respectively, c) power angular profile $P_{\omega}^{(R)}(q)$ and a histogram of the angular spread $S_{\omega}^{(R)}(s_R)$ from 10000 generated samples by the CSVAE and CSGMM compared to ground truth.

pute the corresponding noise variance σ_i^2 in (10). A more detailed description of the datasets, chosen configurations, and pre-processing is given in Appendices H-J.

Evaluation metrics We evaluate the parameter generation performance by the power angular profile

$$P_{\omega}^{(R)}(q) = \frac{1}{N_{\text{test}}} \sum_{i=1}^{N_{\text{test}}} \frac{|s_{R,i}^{(q)}|^2}{\sum_{g=-S_R/2}^{S_R/2-1} |s_{R,i}^{(g)}|^2} \quad (13)$$

as well as the channel-wise angular spread

$$S_{\omega}^{(R)}(s_R) = \sqrt{\frac{\sum_{g=-S_R/2}^{S_R/2-1} (\omega_g^{(R)} - \mu_R^{(g)})^2 |s_{R,i}^{(g)}|^2}{\sum_{g=-S_R/2}^{S_R/2-1} |s_{R,i}^{(g)}|^2}} \quad (14)$$

with $s_{R,i}^{(g)}$ being the g th entry in the i th newly generated sample $s_{R,i}$. Moreover, $\omega_g^{(R)} = g\pi/S_R$ and $\mu_R^{(g)} = (\sum_{g=-S_R/2}^{S_R/2-1} \omega_g^{(R)} |s_{R,i}^{(g)}|^2) / (\sum_{g=-S_R/2}^{S_R/2-1} |s_{R,i}^{(g)}|^2)$ (Zhang et al., 2017). For the channel generation performance, we map newly generated s_R (or $s_{t,f}$) to \mathbf{h} using a dictionary \mathbf{D}_R (or $\mathbf{D}_{t,f}$) (cf. Section 4.1) and evaluate the channel generation with the cross-validation method from (Baur et al., 2024c; Xiao et al., 2022). Specifically, we first train each generative model using (10) and generate $N_{(\text{gen})}$ channels with each model to train an autoencoder for reconstruction by minimizing the mean squared error (MSE) for each generative model separately. We then compress and reconstruct ground-truth (e.g., QuaDRiGa or DeepMIMO) channels using these trained autoencoders and evaluate the normalized MSE (NMSE) $\text{nMSE} = 1/N_{\text{test}} \sum_{i=1}^{N_{\text{test}}} (\|\hat{\mathbf{h}}_i - \mathbf{h}_i\|_2^2 / N)$ and the cosine similarity $\rho_c = 1/N_{\text{test}} \sum_{i=1}^{N_{\text{test}}} (\|\hat{\mathbf{h}}_i^H \mathbf{h}_i\| / (\|\hat{\mathbf{h}}_i\|_2 \|\mathbf{h}_i\|_2))$ with \mathbf{h}_i and $\hat{\mathbf{h}}_i$ being the ground-truth and reconstructed channel.

Baselines & architectures For the parameter generation in SIMO, we compare our method to ground-truth.⁵ For generating channel realizations, we evaluate AmbientGAN (Bora et al., 2018), a GAN variant that can learn on compressed and noisy data. Moreover, for OFDM we use a radial basis function interpolation to estimate the corresponding channel $\hat{\mathbf{h}}_{\text{rbf},i}$ over the whole OFDM grid for each \mathbf{y}_i in (10). We then use this data to train and evaluate a Wasserstein GAN with gradient penalty denoted by GAN-rbf. A detailed overview of all architectures, hyperparameters, and the ground-truth baseline is given in Appendix K.

6.2. Results

Modified 3GPP In Fig. 1 a) and b), exemplary training samples and newly generated samples are shown. In Fig. 1 c), the power angular profile $P_{\omega}^{(R)}(q)$ as well as a histogram of the angular spread $S_{\omega}^{(R)}(s_R)$ is given. The number of antennas $N = M$ is set to 16, and the number of gridpoints S is set to 256. Perceptually, the newly generated samples of CSVAE and CSGMM resemble ground truth. While CSGMM produces a sharper power angular profile with more peaks than ground-truth, it is generally consistent by, e.g., not assigning power to directions absent in the ground-truth profile. The generated power angular profile of CSVAE matches ground truth. Regarding the angular spread, CSGMM slightly overestimates the angular spread, and CSVAE exhibits a few outliers with a large angular spread, but generally, both closely resemble ground truth.

QuaDRiGa In Fig. 2 a)-d), the nMSE and ρ_c of the autoencoder reconstruction is shown over the number N_t of training samples with fixed $M = 50$ for all generative mod-

⁵To the best of our knowledge, there is no alternative method of generating physical parameters for wireless channels based on a training set of compressed and noisy channel observations.

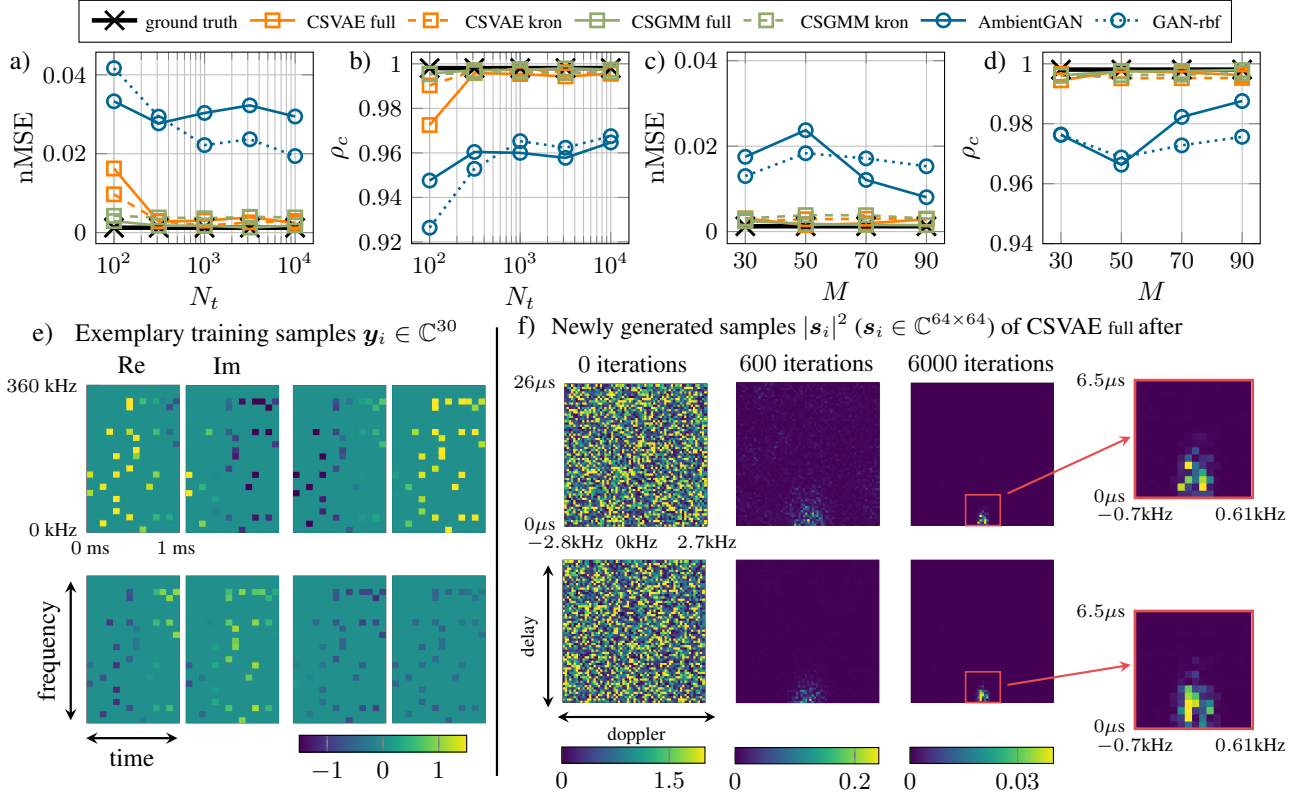


Figure 2. a) - d) nMSE and ρ_c for reconstructing ground-truth channels by an autoencoder trained on channel realizations produced by the generative models, respectively. In a) and b), we vary the number N_t of training samples for the generative models with fixed $M = 50$, and in c) and d), we vary the number M of pilot symbols with fixed $N_t = 10000$. e) four exemplary training samples, f) illustration of the CSVAE full training by plotting the squared absolute value of two generated samples after 0, 600, and 6000 iterations during training.

els, and over the number M of pilot symbols with fixed $N_t = 10000$. In all simulations, $N_{(\text{gen})} = 10000$. We plot the performance of our method without (full) and with (kron) Kronecker approximation (cf. Section 4.4). The training dataset is $\mathcal{Y}_{t,f}^{(\text{SG})}$ (cf. Appendix I) and we choose $S_t = S_f = 64$, $\bar{\tau} = 26\mu\text{s}$ and $\bar{\nu} = 5.6\text{kHz}$ (cf. Section 4.1). In Fig. 2 a)-d), our proposed methods outperform the baselines AmbientGAN and GAN-rbf, and closely approach the ground truth for which the autoencoder has been trained on 10000 QuaDRiGa channel realizations. Fig. 2 e) shows four exemplary training samples. To illustrate the OFDM masking with pilot symbols, we plot the real (Re) and imaginary (Im) part of the 30-dimensional observations within the OFDM grid representing the underlying channel $\mathbf{H} \in \mathbb{C}^{24 \times 14}$ with $\mathbf{h} = \text{vec}(\mathbf{H})$. Fig. 2 f) illustrates the training of CSVAE full for $M = 30$ and $N_t = 10000$. Specifically, we plot the squared absolute value of two samples in the delay-doppler domain after 0, 600, and 6000 training iterations. Since the signals' velocity is the speed of light and the users' maximum distance to the BS is 500m (cf. Appendix I), delays being significantly larger than $1.66\mu\text{s}$ are not to be expected, which is consistent with Fig. 2 f).⁶

⁶Note that delays can exceed $1.66\mu\text{s}$ due to reflections.

Additional Results In Appendix L, we provide results for OFDM with a larger bandwidth and overall duration compared to Fig 2. Moreover, we analyze our proposed model's generalizability to adapt to other system configurations after training (cf. Section 5) and discuss its ability to control the number of generated paths per sample. We also test the parameter and channel generation, and the generalizability for the DeepMIMO ray tracing dataset.

7. Conclusion

In this work, we combined the physics-related compressibility of wireless channels with SBGM and knowledge about conditional channel moments to develop a *prescribed* physics-informed generative model for wireless channels. Our method can generate the physical channel parameters and channel realizations themselves. We have shown that the parameter generation is consistent with ground truth and that our method outperforms GAN-based baselines for generating channel realizations. Limitations, such as generating non-stationary channel trajectories, are part of future work.

References

- 3GPP. 5G;NR; physical channels and modulation (release 16). Technical Report TS 38.211 version 16.2.0 Release 16, 3rd Generation Partnership Project (3GPP), 2020.
- 3GPP. Evolved universal terrestrial radio access (E-UTRA); base station (BS) radio transmission and reception (release 18). Technical Report TS 36.104 version 18.4.0 Release 18, 3rd Generation Partnership Project (3GPP), 2023.
- 3GPP. Study on channel model for frequencies from 0.5 to 100 GHz (release 18). Technical Report TR 38.901 version 18.0.0 Release 18, 3rd Generation Partnership Project (3GPP), 2024a.
- 3GPP. Spatial channel model for multiple input multiple output (MIMO) simulations (release 18). Technical Report TR 25.996 version 18.0.0 Release 18, 3rd Generation Partnership Project (3GPP), 2024b.
- Alkhateeb, A. DeepMIMO: A generic deep learning dataset for millimeter wave and massive MIMO applications. In *Proc. of Information Theory and Applications Workshop (ITA)*, pp. 1–8, San Diego, CA, Feb 2019.
- Almers, P., Bonek, E., Burr, A. G., Czink, N., Debbah, M., Degli-Esposti, V., Hofstetter, H., Kyösti, P., Laurenson, D. I., Matz, G., Molisch, A. F., Oestges, C., and Ozelik, H. Survey of channel and radio propagation models for wireless MIMO systems. *EURASIP J. Wireless Commun. Netw.*, 2007:1–19, 2007.
- Baur, M., Fesl, B., and Utschick, W. Leveraging variational autoencoders for parameterized MMSE estimation. *IEEE Transactions on Signal Processing*, 72:3731–3744, 2024a.
- Baur, M., Turan, N., Fesl, B., and Utschick, W. Channel estimation in underdetermined systems utilizing variational autoencoders. In *ICASSP 2024 - 2024 IEEE International Conference on Acoustics, Speech and Signal Processing (ICASSP)*, pp. 9031–9035, 2024b.
- Baur, M., Turan, N., Wallner, S., and Utschick, W. Evaluation metrics and methods for generative models in the wireless PHY layer, 2024c. arXiv:2408.00634.
- Bello, P. Characterization of randomly time-variant linear channels. *IEEE Trans. on Commun. Syst.*, 11(4):360–393, 1963. doi: 10.1109/TCOM.1963.1088793.
- Bishop, C. M. and Bishop, H. *Deep Learning - Foundations and Concepts*. 1 edition, 2023. ISBN 978-3-031-45468-4.
- Bond-Taylor, S., Leach, A., Long, Y., and Willcocks, C. G. Deep generative modelling: A comparative review of VAEs, GANs, normalizing flows, energy-based and autoregressive models. *IEEE Transactions on Pattern Analysis & Machine Intelligence*, 44(11):7327–7347, nov 2022. ISSN 1939-3539.
- Bora, A., Price, E., and Dimakis, A. G. AmbientGAN: Generative models from lossy measurements. In *6th International Conference on Learning Representations, ICLR 2018, Vancouver, BC, Canada, April 30 - May 3, 2018, Conference Track Proceedings*. OpenReview.net, 2018.
- Böck, B., Baur, M., Rizzello, V., and Utschick, W. Variational inference aided estimation of time varying channels. In *ICASSP 2023 - 2023 IEEE International Conference on Acoustics, Speech and Signal Processing (ICASSP)*, pp. 1–5, 2023.
- Böck, B., Baur, M., Turan, N., Semmler, D., and Utschick, W. A statistical characterization of wireless channels conditioned on side information. *IEEE Wireless Communications Letters*, 13(12):3508–3512, 2024a.
- Böck, B., Syed, S., and Utschick, W. Sparse Bayesian generative modeling for compressive sensing. In *The Thirty-eighth Annual Conference on Neural Information Processing Systems*, 2024b.
- Dai, J. and So, H. C. Real-valued sparse Bayesian learning for doa estimation with arbitrary linear arrays. *IEEE Transactions on Signal Processing*, 69:4977–4990, 2021.
- Diggle, P. J. and Gratton, R. J. Monte carlo methods of inference for implicit statistical models. *Journal of the royal statistical society series b-methodological*, 46:193–212, 1984.
- Doshi, A. S., Gupta, M., and Andrews, J. G. Over-the-air design of GAN training for mmwave MIMO channel estimation. *IEEE Journal on Selected Areas in Information Theory*, 3(3):557–573, 2022.
- Euchner, F., Sanzi, J., Henninger, M., and Ten Brink, S. GAN-based massive MIMO channel model trained on measured data. In *2024 27th International Workshop on Smart Antennas (WSA)*, pp. 109–116, 2024.
- Fesl, B., Turan, N., Joham, M., and Utschick, W. Learning a Gaussian mixture model from imperfect training data for robust channel estimation. *IEEE Wireless Communications Letters*, 12(6):1066–1070, 2023.
- Fesl, B., Turan, N., Böck, B., and Utschick, W. Channel estimation for quantized systems based on conditionally Gaussian latent models. *IEEE Transactions on Signal Processing*, 72:1475–1490, 2024.

- Gan, M., Meissner, P., Mani, F., Leitinger, E., Fröhle, M., Oestges, C., Witrisal, K., and Zemen, T. Calibration of indoor UWB sub-band divided ray tracing using multiobjective simulated annealing. In *2014 IEEE International Conference on Communications (ICC)*, pp. 4844–4849, 2014. doi: 10.1109/ICC.2014.6884087.
- Gaudio, L., Colavolpe, G., and Caire, G. OTFS vs. OFDM in the presence of sparsity: A fair comparison. *IEEE Transactions on Wireless Communications*, 21(6):4410–4423, 2022.
- Geok, T. K., Hossain, F., Kamaruddin, M. N., Abd Rahman, N. Z., Thiagarah, S., Tan, A. W. C., Hossen, J., and Liew, C. P. A comprehensive review of efficient ray-tracing techniques for wireless communication. *Journal on Communications Antenna and Propagation (IRECAP)*, 8:123, 2018.
- Girin, L., Leglaive, S., Bie, X., Diard, J., Hueber, T., and Alameda-Pineda, X. Dynamical Variational Autoencoders: A Comprehensive Review. *Found. Trends Mach. Learn.*, 15(1-2):1–175, 2021.
- Goodfellow, I., Pouget-Abadie, J., Mirza, M., Xu, B., Warde-Farley, D., Ozair, S., Courville, A., and Bengio, Y. Generative adversarial nets. In Ghahramani, Z., Welling, M., Cortes, C., Lawrence, N., and Weinberger, K. (eds.), *Advances in Neural Information Processing Systems*, volume 27. Curran Associates, Inc., 2014.
- Heckel, R. and Hand, P. Deep decoder: Concise image representations from untrained non-convolutional networks. In *7th International Conference on Learning Representations, ICLR 2019, New Orleans, LA, USA, May 6-9, 2019*. OpenReview.net, 2019.
- Hofmann, G. R. Who invented ray tracing? *Vis. Comput.*, 6(3):120–124, may 1990. ISSN 0178-2789.
- Hoydis, J., Aoudia, F. A., Cammerer, S., Euchner, F., Nimier-David, M., Brink, S. T., and Keller, A. Learning radio environments by differentiable ray tracing. *IEEE Transactions on Machine Learning in Communications and Networking*, 2:1527–1539, 2024.
- Hu, Z., Li, Y., and Han, C. Transformer-based GAN for terahertz spatial-temporal channel modeling and generating. In *2023 IEEE Globecom Workshops (GC Wkshps)*, pp. 1916–1921, 2023. doi: 10.1109/GCWkshps58843.2023.10464580.
- Imoize, A. L., Ibhaze, A. E., Atayero, A. A., and Kavitha, K. V. N. Standard propagation channel models for MIMO communication systems. *Wireless Communications and Mobile Computing*, 2021(1):8838792, 2021.
- Jaeckel, S., Raschkowski, L., Börner, K., and Thiele, L. Quadriga: A 3-D multi-cell channel model with time evolution for enabling virtual field trials. *IEEE Trans. Antennas Propag.*, 62(6):3242–3256, 2014.
- Jaeckel, S., Raschkowski, L., Börner, K., Thiele, L., Burkhard, F., and Ernst, E. QuaDRiGa - quasi deterministic radio channel generator, user manual and documentation. Technical Report Tech. Rep. v2.8.1, Fraunhofer Heinrich Hertz Institute, 2023.
- Karniadakis, G. E., Kevrekidis, I. G., Lu, L., Perdikaris, P., Wang, S., and Yang, L. Physics-informed machine learning. *Nature Reviews Physics*, 3(6), 5 2021. ISSN 2522-5820.
- Kim, W., Ahn, Y., Kim, J., and Shim, B. Towards deep learning-aided wireless channel estimation and channel state information feedback for 6G. *Journal of Communications and Networks*, 25(1):61–75, 2023.
- Kingma, D. P. and Ba, J. Adam: A Method for Stochastic Optimization. In *3rd International Conference on Learning Representations 2015*, 2015.
- Kingma, D. P. and Welling, M. Auto-encoding variational Bayes. In *2nd International Conference on Learning Representations, ICLR 2014, Banff, AB, Canada, April 14-16, 2014, Conference Track Proceedings*, 2014.
- Koller, M., Fesl, B., Turan, N., and Utschick, W. An asymptotically MSE-optimal estimator based on Gaussian mixture models. *IEEE Transactions on Signal Processing*, 70:4109–4123, 2022.
- Lee, T., Park, J., Kim, H., and Andrews, J. G. Generating high dimensional user-specific wireless channels using diffusion models, 2024. arXiv:2409.03924.
- Li, X., Alkhateeb, A., and Tepedelenlioğlu, C. Generative adversarial estimation of channel covariance in vehicular millimeter wave systems. In *2018 52nd Asilomar Conference on Signals, Systems, and Computers*, pp. 1572–1576, 2018.
- Liu, L., Poutanen, J., Quitin, F., Haneda, K., Tufvesson, F., Doncker, P., Vainikainen, P., and Oestges, C. The COST 2100 MIMO channel model. *IEEE Wireless Communications*, 19:92–99, 12 2012. doi: 10.1109/MWC.2012.6393523.
- McKown, J. and Hamilton, R. Ray tracing as a design tool for radio networks. *IEEE Network*, 5(6):27–30, 1991.
- Meinilä, J., Kyösti, P., Jämsä, T., and Hentilä, L. *WINNER II Channel Models*, chapter 3, pp. 39–92. John Wiley & Sons, Ltd, 2009. ISBN 9780470748077.

- Mohamed, S. and Lakshminarayanan, B. Learning in implicit generative models, 2017. arXiv:1610.03483.
- Neumann, D., Wiese, T., and Utschick, W. Learning the MMSE channel estimator. *IEEE Transactions on Signal Processing*, 66(11):2905–2917, 2018.
- Orekondy, T., Behboodi, A., and Soriaga, J. B. MIMO-GAN: Generative MIMO channel modeling. In *ICC 2022 - IEEE International Conference on Communications*, pp. 5322–5328, 2022.
- Orekondy, T., Kumar, P., Kadambi, S., Ye, H., Soriaga, J., and Behboodi, A. WineRT: Towards neural ray tracing for wireless channel modelling and differentiable simulations. In *The Eleventh International Conference on Learning Representations*, 2023.
- Raissi, M., Perdikaris, P., and Karniadakis, G. Physics-informed neural networks: A deep learning framework for solving forward and inverse problems involving nonlinear partial differential equations. *Journal of Computational Physics*, 378:686–707, 2019. ISSN 0021-9991.
- Remcom. Wireless InSite. <http://www.remcom.com/wireless-insite>.
- Rizzello, V. and Utschick, W. Learning the CSI denoising and feedback without supervision. In *2021 IEEE 22nd International Workshop on Signal Processing Advances in Wireless Communications (SPAWC)*, pp. 16–20, 2021.
- Sengupta, U., Jao, C., Bernacchia, A., Vakili, S., and Shiu, D.-s. Generative diffusion models for radio wireless channel modelling and sampling. In *GLOBECOM 2023 - 2023 IEEE Global Communications Conference*, pp. 4779–4784, 2023.
- Seyedsalehi, S., Pourahmadi, V., Sheikhzadeh, H., and Foumani, A. H. G. Propagation channel modeling by deep learning techniques, 2019. arXiv:1908.06767.
- Tian, Y., Li, H., Zhu, Q., Mao, K., Ali, F., Chen, X., and Zhong, W. Generative network-based channel modeling and generation for air-to-ground communication scenarios. *IEEE Communications Letters*, 28(4):892–896, 2024.
- Tipping, M. Sparse Bayesian learning and relevance vector machine. *J. Mach. Learn. Res.*, 1:211–244, 01 2001.
- Tse, D. and Viswanath, P. *Fundamentals of wireless communication*. Cambridge University Press, USA, 2005. ISBN 0521845270.
- Turan, N., Böck, B., Chan, K. J., Fesl, B., Burmeister, F., Joham, M., Fettweis, G., and Utschick, W. Wireless channel prediction via Gaussian mixture models. In *2024 27th International Workshop on Smart Antennas (WSA)*, pp. 1–5, 2024a.
- Turan, N., Fesl, B., Koller, M., Joham, M., and Utschick, W. A versatile low-complexity feedback scheme for FDD systems via generative modeling. *IEEE Transactions on Wireless Communications*, 23(6):6251–6265, 2024b.
- Turan, N., Böck, B., Fesl, B., Joham, M., Gündüz, D., and Utschick, W. A versatile pilot design scheme for FDD systems utilizing Gaussian mixture models. *IEEE Transactions on Wireless Communications*, pp. 1–1, 2025. doi: 10.1109/TWC.2025.3537496. early access.
- Wang, C.-X., Bian, J., Sun, J., Zhang, W., and Zhang, M. A survey of 5G channel measurements and models. *IEEE Communications Surveys & Tutorials*, 20(4):3142–3168, 2018.
- Wang, C.-X., Huang, J., Wang, H., Gao, X., You, X., and Hao, Y. 6G wireless channel measurements and models: Trends and challenges. *IEEE Vehicular Technology Magazine*, 15(4):22–32, 2020.
- Wipf, D. and Rao, B. Sparse Bayesian learning for basis selection. *IEEE Transactions on Signal Processing*, 52(8):2153–2164, 2004.
- Xia, W., Rangan, S., Mezzavilla, M., Lozano, A., Geraci, G., Semkin, V., and Loianno, G. Generative neural network channel modeling for millimeter-wave UAV communication. *IEEE Transactions on Wireless Communications*, 21(11):9417–9431, 2022. doi: 10.1109/TWC.2022.3176480.
- Xiao, H., Tian, W., Liu, W., and Shen, J. Channelgan: Deep learning-based channel modeling and generating. *IEEE Wireless Communications Letters*, 11(3):650–654, 2022.
- Yang, Y., Li, Y., Zhang, W., Qin, F., Zhu, P., and Wang, C.-X. Generative-adversarial-network-based wireless channel modeling: Challenges and opportunities. *IEEE Commun. Mag.*, 57(3):22–27, 2019.
- Yin, X. and Cheng, X. *Propagation Channel Characterization, Parameter Estimation, and Modeling for Wireless Communication*. Wiley-IEEE Press, November 2016.
- Yun, Z. and Iskander, M. F. Ray tracing for radio propagation modeling: Principles and applications. *IEEE Access*, 3:1089–1100, 2015.
- Zhang, R., Lu, X., Zhao, J., Cai, L., and Wang, J. Measurement and modeling of angular spreads of three-dimensional urban street radio channels. *IEEE Transactions on Vehicular Technology*, 66(5):3555–3570, 2017.

A. Channel Sparsity in OFDM Systems

The OFDM channel matrix is given by (3), i.e.,

$$\mathbf{H} = \sum_{\ell=1}^L \sum_{m=1}^{M_\ell} \rho_{\ell,m} \mathbf{a}_t(\vartheta_{\ell,m}) \mathbf{a}_f(\tau_{\ell,m})^T \quad (15)$$

with $\mathbf{a}_t(\vartheta_{\ell,m})|_i = e^{-j2\pi\vartheta_{\ell,m}(i-1)\Delta T}$ and $\mathbf{a}_f(\tau_{\ell,m})|_j = e^{-j2\pi\tau_{\ell,m}(j-1)\Delta f}$.⁷ We assume that we have access to (not necessarily tight) upper bounds $\bar{\tau}$ and $\bar{\vartheta}/2$ for all delays and doppler shifts, i.e.,

$$\max_{\ell,m} \tau_{\ell,m} < \bar{\tau} \quad (16)$$

$$\max_{\ell,m} |\vartheta_{\ell,m}| \leq \bar{\vartheta}/2 \quad (17)$$

By deciding for a number of grid points S_f and S_t in the delay and doppler domain, respectively, we define the grids $\mathcal{G}_f = \{j\bar{\tau}/S_f\}_{j=0}^{S_f-1}$ as well as $\mathcal{G}_t = \{i\bar{\vartheta}/S_t\}_{i=-S_t/2}^{S_t/2-1}$. In consequence, we can represent the OFDM channel matrix in (15) using $\mathcal{G}_f \times \mathcal{G}_t$ as

$$\mathbf{h} = \sum_{i=-S_t/2}^{S_t/2-1} \sum_{j=0}^{S_f-1} s_{t,f}^{(i,j)} \text{vec} \left(\mathbf{a}_t\left(\frac{i\bar{\vartheta}}{S_t}\right) \mathbf{a}_f\left(\frac{j\bar{\tau}}{S_f}\right)^T \right) = \mathbf{D}_{t,f} \mathbf{s}_{t,f}, \quad (18)$$

with $\mathbf{s}_{t,f} = \text{vec}(\mathbf{S}_{t,f})$, $\mathbf{S}_{t,f}|_{i,j} = s_{t,f}^{(i,j)}$ and $\mathbf{D}_{t,f} = \mathbf{D}_t \otimes \mathbf{D}_f$. Moreover,

$$\mathbf{D}_t = [\mathbf{a}_t(-\frac{\bar{\vartheta}}{2}), \dots, \mathbf{a}_t(\frac{\bar{\vartheta}}{2} - \frac{\bar{\vartheta}}{S_t})] \quad (19)$$

$$\mathbf{D}_f = [\mathbf{a}_f(0), \dots, \mathbf{a}_f(\bar{\tau} - \frac{\bar{\tau}}{S_f})] \quad (20)$$

and we know $\mathbf{s}_{t,f}$ to be compressible in general.

B. Detailed Explanation for the Preservation of the Zero-Mean Toeplitz-Covariance Structure by CGLMs

To understand why the statistical model in (7)-(9) aligns with the inherent properties of wireless channels and, thus, is suited for generating wireless channels, we need to combine three arguments.

- The complex path losses $\rho_{\ell,m}$ in (1) model several physical as well as technical effects contributing to the wireless channel, such as the antennas' radiation patterns or changes in polarization due to reflections (Jaeckel et al., 2023). However, their phases also contain the phase shift due to the center frequency modulation, i.e., $2\pi f_c \tau_{\ell,m}$ with f_c being the center frequency (Tse & Viswanath, 2005). We reformulate $f_c \tau_{\ell,m} = d_{\ell,m}/\lambda_c$ with $d_{\ell,m}$ being the (sub-)path length between the transmitter and receiver (cf. (1)), and λ_c being the corresponding wavelength (i.e., $c = \lambda_c f_c$ with the speed of light c). Typical center frequencies f_c for the wireless transmission of signals range from a few GHz to tens or even hundreds of GHz. Thus, the corresponding wavelength λ_c takes values of at most a few centimeters or smaller. Consequently, by just changing the (sub-)path length by λ_c (i.e., a few centimeters or less), the path loss phase $\arg(\rho_{\ell,m})$ takes a full turn of 2π , or, in other words, by just slight movements of users, the path loss phases $\arg(\rho_{\ell,m})$ rapidly change. Since we want to statistically describe the wireless channel over a whole scenario whose dimensions are much larger than the center wavelength and, thus, lead to $d_{\ell,m} \gg \lambda_c$, the path loss phases $\arg(\rho_{\ell,m})$ are generally modeled to be uniformly distributed (Tse & Viswanath, 2005).
- When choosing the dimension of the latent variable \mathbf{z} in CGLMs (e.g., VAEs) to be smaller than the dimension of the data whose distribution the CGLM is supposed to be learned, the training of the CGLM aims to train \mathbf{z} to be a statistically meaningful (lower-dimensional) representation of the data of interest (Bishop & Bishop, 2023).

⁷The term $\mathbf{a}_R(\boldsymbol{\Omega}_{\ell,m}^{(R)}) \mathbf{a}_T(\boldsymbol{\Omega}_{\ell,m}^{(T)})^T$ is also sometimes represented by its equivalent tensor product $\mathbf{a}_R(\boldsymbol{\Omega}_{\ell,m}^{(R)}) \otimes \mathbf{a}_T(\boldsymbol{\Omega}_{\ell,m}^{(T)})$, cf. (Böck et al., 2024a).

- By building on a probabilistic graph representation of wireless channels, the work in (Böck et al., 2024a) proves that if a variable does not contain any information about the complex path loss phases $\arg(\rho_{\ell,m})$, the conditioning on this variable preserves the structural properties of channel moments, i.e., the channel's zero mean and Toeplitz covariance structure.

By combining these three arguments, (Böck et al., 2024a) reasons and experimentally validates that the latent variable \mathbf{z} of CGLMs is trained to not capture $\arg(\rho_{\ell,m})$ -related information as these phases do not contain distinct statistically characteristic channel features. In other words, (Böck et al., 2024a) shows that the usual statistical model of CGLMs, i.e.,

$$p_{\theta,\delta}(\mathbf{x}) = \int p_{\theta}(\mathbf{x}|\mathbf{z})p_{\delta}(\mathbf{z})d\mathbf{z} = \int \mathcal{N}_{\mathbb{C}}(\mathbf{x}; \boldsymbol{\mu}_{\theta}(\mathbf{z}), \mathbf{C}_{\theta}(\mathbf{z}))p_{\delta}(\mathbf{z})d\mathbf{z} \quad (21)$$

is learned to fulfill $\boldsymbol{\mu}_{\theta}(\mathbf{z}) = \mathbf{0}$ and $\mathbf{C}_{\theta}(\mathbf{z})$ being (block-)Toeplitz structured when being properly trained on channel realizations. Moreover, we use (8) and (9) as the statistical model for the compressible representation \mathbf{s}_R (or $\mathbf{s}_{t,f}$). By that, we implicitly model \mathbf{h} to be distributed according to a CGLM with

$$p_{\theta,\delta}(\mathbf{h}) = \int p_{\theta}(\mathbf{h}|\mathbf{z})p_{\delta}(\mathbf{z})d\mathbf{z} = \int \mathcal{N}_{\mathbb{C}}(\mathbf{h}; \mathbf{0}, \mathbf{D}_R \text{diag}(\boldsymbol{\gamma}_{\theta}(\mathbf{z}))\mathbf{D}_R^H)p_{\delta}(\mathbf{z})d\mathbf{z} \quad (22)$$

and $\mathbf{D}_R \text{diag}(\boldsymbol{\gamma}_{\theta}(\mathbf{z}))\mathbf{D}_R$ being Toeplitz (or block-Toeplitz when using $\mathbf{D}_{t,f}$), which perfectly aligns with the findings from (Böck et al., 2024a).

C. Closed-Form Moments of $p_{\theta}(\mathbf{s}|\mathbf{z}, \mathbf{y})$

The distribution $p_{\theta}(\mathbf{s}|\mathbf{z}, \mathbf{y})$ forms a conditioned conjugate prior of $\mathbf{y}|\mathbf{s}$ (conditioned on \mathbf{z}). Thus, we can compute the moments of $p_{\theta}(\mathbf{s}|\tilde{\mathbf{z}}_i, \mathbf{y}_i)$ as (see Appendix I in (Böck et al., 2024b))

$$\boldsymbol{\mu}_{\theta}^{\mathbf{s}|\mathbf{y}_i, \tilde{\mathbf{z}}_i}(\tilde{\mathbf{z}}_i) = \mathbf{C}_{\theta}^{\mathbf{s}, \mathbf{y}_i|\tilde{\mathbf{z}}_i}(\tilde{\mathbf{z}}_i) \left(\mathbf{C}_{\theta}^{\mathbf{y}_i|\tilde{\mathbf{z}}_i}(\tilde{\mathbf{z}}_i) \right)^{-1} \mathbf{y}_i \quad (23)$$

$$\mathbf{C}_{\theta}^{\mathbf{s}|\mathbf{y}_i, \tilde{\mathbf{z}}_i}(\tilde{\mathbf{z}}_i) = \text{diag}(\boldsymbol{\gamma}_{\theta}(\tilde{\mathbf{z}}_i)) - \mathbf{C}_{\theta}^{\mathbf{s}, \mathbf{y}_i|\tilde{\mathbf{z}}_i}(\tilde{\mathbf{z}}_i) \left(\mathbf{C}_{\theta}^{\mathbf{y}_i|\tilde{\mathbf{z}}_i}(\tilde{\mathbf{z}}_i) \right)^{-1} \mathbf{C}_{\theta}^{\mathbf{s}, \mathbf{y}_i|\tilde{\mathbf{z}}_i}(\tilde{\mathbf{z}}_i)^H \quad (24)$$

with

$$\mathbf{C}_{\theta}^{\mathbf{y}_i|\tilde{\mathbf{z}}_i}(\tilde{\mathbf{z}}_i) = \mathbf{A}\mathbf{D}\text{diag}(\boldsymbol{\gamma}_{\theta}(\tilde{\mathbf{z}}_i))\mathbf{D}^H\mathbf{A}^H + \sigma_i^2\mathbf{I}, \quad (25)$$

and $\mathbf{C}_{\theta}^{\mathbf{s}, \mathbf{y}_i|\tilde{\mathbf{z}}_i}(\tilde{\mathbf{z}}_i) = \text{diag}(\boldsymbol{\gamma}_{\theta}(\tilde{\mathbf{z}}_i))\mathbf{D}^H\mathbf{A}^H$. Minor differences to the setup in (Böck et al., 2024b) are the sample-dependent noise variance σ_i^2 in (25) as well as taking the hermitian instead of the transpose.

D. Closed Forms for the CSVAE Objective

The objective (11) for CSVAEs consists of three terms, i.e., $\mathbb{E}_{p_{\theta}(\mathbf{s}|\tilde{\mathbf{z}}_i, \mathbf{y}_i)}[\log p(\mathbf{y}_i|\mathbf{s})]$, $D_{\text{KL}}(q_{\phi}(z|\mathbf{y}_i)||p(z))$ and $D_{\text{KL}}(p_{\theta}(\mathbf{s}|\tilde{\mathbf{z}}_i, \mathbf{y}_i)||p_{\theta}(\mathbf{s}|\tilde{\mathbf{z}}_i))$. The second is given by (Kingma & Welling, 2014)

$$D_{\text{KL}}(q_{\phi}(z|\mathbf{y}_i)||p(z)) = -\frac{1}{2} \sum_{j=1}^{N_L} (1 + \log \sigma_{j,\phi}^2(\mathbf{y}_i) - \mu_{j,\phi}(\mathbf{y}_i) - \sigma_{j,\phi}^2(\mathbf{y}_i)) \quad (26)$$

with $q_{\phi}(z|\mathbf{y}_i) = \mathcal{N}(z; \boldsymbol{\mu}_{\phi}(\mathbf{y}_i), \text{diag}(\boldsymbol{\sigma}_{\phi}^2(\mathbf{y}_i)))$ and $\mu_{j,\phi}(\mathbf{y}_i)$ and $\sigma_{j,\phi}^2(\mathbf{y}_i)$ being the j th entry of $\boldsymbol{\mu}_{\phi}(\mathbf{y}_i)$ and $\boldsymbol{\sigma}_{\phi}^2(\mathbf{y}_i)$, respectively. Moreover, N_L is the CSVAE's latent dimension. Separate closed-form solutions for the first and third term in the real-valued case with constant noise variance are given in (Böck et al., 2024b). When adjusting the derivation to the complex-valued case with varying noise covariances σ_i^2 , both terms equal

$$\mathbb{E}_{p_{\theta}(\mathbf{s}|\tilde{\mathbf{z}}_i, \mathbf{y}_i)}[\log p(\mathbf{y}_i|\mathbf{s})] = -\left(M \log(\pi\sigma^2) + \frac{1}{\sigma_i^2} \left(\|\mathbf{y}_i - \mathbf{A}\mathbf{D}\boldsymbol{\mu}_{\theta}^{\mathbf{s}|\mathbf{y}_i, \tilde{\mathbf{z}}_i}(\tilde{\mathbf{z}}_i)\|_2^2 + \text{tr}(\mathbf{A}\mathbf{D}\mathbf{C}_{\theta}^{\mathbf{s}|\mathbf{y}_i, \tilde{\mathbf{z}}_i}(\tilde{\mathbf{z}}_i)\mathbf{D}^H\mathbf{A}^H) \right) \right) \quad (27)$$

and

$$\begin{aligned} D_{\text{KL}}(p_{\theta}(\mathbf{s}|\tilde{\mathbf{z}}_i, \mathbf{y}_i)||p_{\theta}(\mathbf{s}|\tilde{\mathbf{z}}_i)) &= \left(\log \det(\text{diag}(\boldsymbol{\gamma}_{\theta}(\tilde{\mathbf{z}}_i))) - \log \det\left(\mathbf{C}_{\theta}^{\mathbf{s}|\mathbf{y}_i, \tilde{\mathbf{z}}_i}(\tilde{\mathbf{z}}_i)\right) - S \right. \\ &\quad \left. + \text{tr}\left(\text{diag}\left((\boldsymbol{\gamma}_{\theta}(\tilde{\mathbf{z}}_i))^{-1}\right)\mathbf{C}_{\theta}^{\mathbf{s}|\mathbf{y}_i, \tilde{\mathbf{z}}_i}(\tilde{\mathbf{z}}_i)\right) + \boldsymbol{\mu}_{\theta}^{\mathbf{s}|\mathbf{y}_i, \tilde{\mathbf{z}}_i}(\tilde{\mathbf{z}}_i)^H \text{diag}\left(\boldsymbol{\gamma}_{\theta}(\tilde{\mathbf{z}}_i)^{-1}\right)\boldsymbol{\mu}_{\theta}^{\mathbf{s}|\mathbf{y}_i, \tilde{\mathbf{z}}_i}(\tilde{\mathbf{z}}_i) \right) \end{aligned} \quad (28)$$

where $\boldsymbol{\mu}_\theta^{s|\mathbf{y}_i, \tilde{\mathbf{z}}_i}(\tilde{\mathbf{z}}_i)$ and $\mathbf{C}_\theta^{s|\mathbf{y}_i, \tilde{\mathbf{z}}_i}(\tilde{\mathbf{z}}_i)$ are the mean and covariance matrix of $p_\theta(\mathbf{s}|\tilde{\mathbf{z}}_i, \mathbf{y}_i)$ (cf. (23) and (24)). Moreover, (Böck et al., 2024b) reformulates both terms and shows that they partially cancel out, leading to a more efficient computation, i.e.,

$$\begin{aligned} \mathbb{E}_{p_\theta(\mathbf{s}|\tilde{\mathbf{z}}_i, \mathbf{y}_i)}[\log p(\mathbf{y}_i|\mathbf{s})] - \text{D}_{\text{KL}}(p_\theta(\mathbf{s}|\tilde{\mathbf{z}}_i, \mathbf{y}_i)||p_\theta(\mathbf{s}|\tilde{\mathbf{z}}_i)) &= -\left(M \log(\pi\sigma_i^2) + \frac{1}{\sigma_i^2} \left(\|\mathbf{y}_i - \mathbf{A}\mathbf{D}\boldsymbol{\mu}_\theta^{s|\mathbf{y}_i, \tilde{\mathbf{z}}_i}(\tilde{\mathbf{z}}_i)\|_2^2\right)\right) \\ &\quad - \left(M \log \sigma_i^2 + \log \det \mathbf{C}_\theta^{s|\mathbf{y}_i, \tilde{\mathbf{z}}_i}(\tilde{\mathbf{z}}_i) + \boldsymbol{\mu}_\theta^{s|\mathbf{y}_i, \tilde{\mathbf{z}}_i}(\tilde{\mathbf{z}}_i)^{\text{H}} \text{diag}(\boldsymbol{\gamma}_\theta(\tilde{\mathbf{z}}_i)^{-1}) \boldsymbol{\mu}_\theta^{s|\mathbf{y}_i, \tilde{\mathbf{z}}_i}(\tilde{\mathbf{z}}_i)\right) \end{aligned} \quad (29)$$

Note that due to having complex-valued Gaussians, (29) differs slightly from the terms in (Böck et al., 2024b).

E. E-step and M-step for the CSGMM

E-step Generally, the E-step corresponds to computing the model's posterior $p(\mathbf{s}, k|\mathbf{y}_i) = p(\mathbf{s}|k, \mathbf{y}_i)p(k|\mathbf{y}_i)$ for each training sample \mathbf{y}_i . Equivalent to the CSVAE, $p(\mathbf{s}|k, \mathbf{y}_i)$ is Gaussian whose mean and covariance can be computed via (23) and (24). Moreover, $p(k|\mathbf{y}_i)$ can be calculated using Bayes, i.e.,

$$p(k|\mathbf{y}_i) = \frac{p(\mathbf{y}_i|k)p(k)}{\sum_k p(\mathbf{y}_i|k)p(k)}. \quad (30)$$

Due to modeling $\mathbf{s}|k$ to be a zero-mean Gaussian and \mathbf{y} being linearly dependent on \mathbf{s} (cf. Section 4.2), the distribution $p(\mathbf{y}_i|k)$ is a zero-mean Gaussian with covariance matrix (cf. (25))

$$\mathbf{C}_k^{\mathbf{y}_i|k} = \mathbf{A}\mathbf{D}\text{diag}(\boldsymbol{\gamma}_k)\mathbf{D}^{\text{H}}\mathbf{A}^{\text{H}} + \sigma_i^2\mathbf{I}. \quad (31)$$

Thus, (30) is computable in closed form.

M-step The M-step for the $(u+1)$ th iteration for CSGMMs solves

$$\{\rho_{k,(u+1)}, \boldsymbol{\gamma}_{k,(u+1)}\} = \underset{\{\rho_k, \boldsymbol{\gamma}_k\}}{\text{argmax}} \sum_{\mathbf{y}_i \in \mathcal{Y}} \mathbb{E}_{p_u(k, \mathbf{s}|\mathbf{y}_i)}[\log p(\mathbf{y}_i, \mathbf{s}, k)] \quad \text{s.t.} \quad \sum_k \rho_k = 1. \quad (32)$$

with $p_u(k, \mathbf{s}|\mathbf{y}_i)$ being the posterior for the i th training sample computed in the u th iteration of the EM algorithm. The closed-form solution is given by (Böck et al., 2024b)

$$\boldsymbol{\gamma}_{k,(u+1)} = \frac{\sum_{\mathbf{y}_i \in \mathcal{Y}} p_u(k|\mathbf{y}_i)(\|\boldsymbol{\mu}_{k,u}^{s|\mathbf{y}_i,k}\|_2^2 + \text{diag}(\mathbf{C}_{k,u}^{s|\mathbf{y}_i,k}))}{\sum_{\mathbf{y}_i \in \mathcal{Y}} p_u(k|\mathbf{y}_i)} \quad (33)$$

$$\rho_{k,(u+1)} = \frac{\sum_{\mathbf{y}_i \in \mathcal{Y}} p_u(k|\mathbf{y}_i)}{|\mathcal{Y}|}. \quad (34)$$

F. Coordinate Search Closed-Form Solutions for the CSGMM M-step with Kronecker Constraint

We aim solve (32) with the constraint $\boldsymbol{\gamma}_k = \boldsymbol{\gamma}_k^{(t)} \otimes \boldsymbol{\gamma}_k^{(f)}$. Following the derivation in Appendix F of (Böck et al., 2024b) and considering that we have complex-valued Gaussians, we reformulate the optimization problem as

$$\begin{aligned} \underset{\{\rho_k, \boldsymbol{\gamma}_k\}}{\text{argmax}} \quad & \sum_{\mathbf{y}_i \in \mathcal{Y}} \sum_{k=1}^K p_u(k|\mathbf{y}_i) \left(- \left(S \log \pi + \sum_{j=1}^S \left(\log \gamma_{k,j} + \frac{\|\boldsymbol{\mu}_{k,j}^{s|\mathbf{y}_i,k}\|_2^2 + \mathbf{C}_{k,j,j}^{s|\mathbf{y}_i,k}}{\gamma_{k,j}} \right) \right) + \log \rho_k \right) \\ \text{s.t.} \quad & \sum_k \rho_k = 1, \quad \boldsymbol{\gamma}_k = \boldsymbol{\gamma}_k^{(t)} \otimes \boldsymbol{\gamma}_k^{(f)} \text{ for all } k \end{aligned} \quad (35)$$

with $S = S_t \cdot S_f$ and $\boldsymbol{\mu}_{k,j}^{s|\mathbf{y}_i,k}$ and $\mathbf{C}_{k,j,j}^{s|\mathbf{y}_i,k}$ denote the j th entry of $\boldsymbol{\mu}_{k,u}^{s|\mathbf{y}_i,k}$ and the diagonal of $\mathbf{C}_{k,u}^{s|\mathbf{y}_i,k}$ in the u th iteration, respectively. By defining $r(q, p) = (q-1)S_f + p$, we can rewrite

$$\boldsymbol{\gamma}_{k,r(q,p)} = \boldsymbol{\gamma}_{k,q}^{(t)} \cdot \boldsymbol{\gamma}_{k,p}^{(f)} \quad (36)$$

and, thus, (35) can be rewritten as

$$\begin{aligned} \operatorname{argmax}_{\{\rho_k, \gamma_k\}} \sum_{\mathbf{y}_i \in \mathcal{Y}} \sum_{k=1}^K p_u(k|\mathbf{y}_i) & \left(-S \log \pi - S_f \sum_{q=1}^{S_t} \log \gamma_{k,q}^{(t)} - S_t \sum_{p=1}^{S_f} \log \gamma_{k,p}^{(f)} - \sum_{q,p=1}^{S_t, S_f} \frac{|\mu_{k,r(q,p)}^{\mathbf{s}|\mathbf{y}_i,k}|^2 + C_{k,r(q,p),r(q,p)}^{\mathbf{s}|\mathbf{y}_i,k}}{\gamma_{k,q}^{(t)} \cdot \gamma_{k,p}^{(f)}} + \log \rho_k \right) \\ \text{s.t. } \sum_k \rho_k & = 1 \end{aligned} \quad (37)$$

The corresponding Lagrangian \mathcal{L} is given by

$$\begin{aligned} \mathcal{L} = \sum_{\mathbf{y}_i \in \mathcal{Y}} \sum_{k=1}^K p_u(k|\mathbf{y}_i) & \left(-S \log \pi - S_f \sum_{q=1}^{S_t} \log \gamma_{k,q}^{(t)} - S_t \sum_{p=1}^{S_f} \log \gamma_{k,p}^{(f)} - \sum_{q,p=1}^{S_t, S_f} \frac{|\mu_{k,r(q,p)}^{\mathbf{s}|\mathbf{y}_i,k}|^2 + C_{k,r(q,p),r(q,p)}^{\mathbf{s}|\mathbf{y}_i,k}}{\gamma_{k,q}^{(t)} \cdot \gamma_{k,p}^{(f)}} + \right. \\ & \left. \log \rho_k \right) + \nu \left(1 - \sum_k \rho_k \right) \end{aligned} \quad (38)$$

with Lagrangian multiplier ν . In the following, we consider coordinate search, i.e., we keep $\{\gamma_k^{(f)}\}_{k=1}^K$ fixed and solely optimize over $\{\gamma_k^{(t)}\}_{k=1}^K$ (and vice versa). By taking the derivative of \mathcal{L} with respect to $\gamma_{\bar{k},\bar{q}}^{(t)}$ and setting it to zero, we end up with

$$\frac{\partial}{\partial \gamma_{\bar{k},\bar{q}}^{(t)}} \mathcal{L} = \sum_{\mathbf{y}_i \in \mathcal{Y}} p_u(\bar{k}|\mathbf{y}_i) \left(-\frac{S_f}{\gamma_{\bar{k},\bar{q}}^{(t)}} + \sum_{p=1}^{S_f} \frac{|\mu_{\bar{k},r(\bar{q},p)}^{\mathbf{s}|\mathbf{y}_i,\bar{k}}|^2 + C_{\bar{k},r(\bar{q},p),r(\bar{q},p)}^{\mathbf{s}|\mathbf{y}_i,\bar{k}}}{\gamma_{\bar{k},\bar{q}}^{(t)2} \gamma_{\bar{k},p}^{(f)}} \right) = 0 \quad (39)$$

and, thus,

$$\gamma_{\bar{k},\bar{q}}^{(t)} = \sum_{p=1}^{S_f} \frac{\sum_{i=1}^{N_t} p_u(\bar{k}|\mathbf{y}_i) \left(|\mu_{\bar{k},r(\bar{q},p)}^{\mathbf{s}|\mathbf{y}_i,\bar{k}}|^2 + C_{\bar{k},r(\bar{q},p),r(\bar{q},p)}^{\mathbf{s}|\mathbf{y}_i,\bar{k}} \right)}{S_f \gamma_{\bar{k},p}^{(f)} \sum_{i=1}^{N_t} p(\bar{k}|\mathbf{y}_i)} \quad (40)$$

for all $\bar{q} = 1, \dots, S_t$, $\bar{k} = 1, \dots, K$. Due to the symmetry of (37) with respect to $\gamma_k^{(t)}$ and $\gamma_k^{(f)}$, we find an equivalent update for $\gamma_k^{(f)}$, i.e.,

$$\gamma_{\bar{k},\bar{p}}^{(f)} = \sum_{q=1}^{S_t} \frac{\sum_{i=1}^{N_t} p_u(\bar{k}|\mathbf{y}_i) \left(|\mu_{\bar{k},r(q,\bar{p})}^{\mathbf{s}|\mathbf{y}_i,\bar{k}}|^2 + C_{\bar{k},r(q,\bar{p}),r(q,\bar{p})}^{\mathbf{s}|\mathbf{y}_i,\bar{k}} \right)}{S_t \gamma_{\bar{k},q}^{(t)} \sum_{i=1}^{N_t} p(\bar{k}|\mathbf{y}_i)} \quad (41)$$

for all $\bar{p} = 1, \dots, S_f$, $\bar{k} = 1, \dots, K$. We suppressed the index for the coordinate search due to readability. The update steps of the weights $\{\rho_k\}_{k=1}^K$ equal those in (Böck et al., 2024b) and are given by

$$\rho_{\bar{k}} = \frac{\sum_{\mathbf{y}_i \in \mathcal{Y}} p_u(\bar{k}|\mathbf{y}_i)}{\nu} \quad (42)$$

$$\nu = |\mathcal{Y}| \quad (43)$$

G. Limitations

Our proposed method exhibits some limitations, which are discussed below.

Non-Stationary Channel Generation When modeling the wireless channel using its compressible representation (6) and (18), one assumption is that each dictionary column only depends on one single grid point. More precisely, in SIMO, each column $\mathbf{a}_R(\frac{y\pi}{S_R})$ corresponds to only one single angle $\frac{y\pi}{S_R}$. From a physical perspective, this means that at each antenna, the impinging waveform comes from the exact same direction. This is called the far-field approximation and is a common assumption in radar and wireless communications exploiting multiple antennas (Yin & Cheng, 2016). From a statistical perspective, the far-field approximation leads to a spatially stationary process. Equivalently, in OFDM, each dictionary column in (18) only corresponds to a single delay-doppler tuple $(j\bar{\tau}/S_f, i\bar{\nu}/S_t)$. Thus, each timestamp and subcarrier in

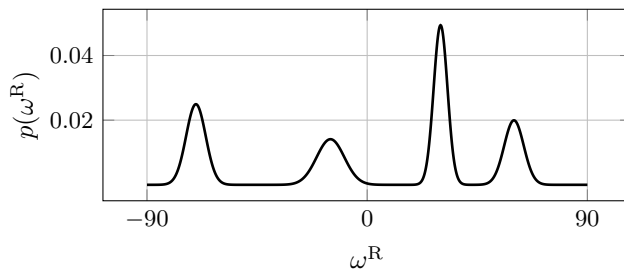


Figure 3. Distribution $p(\omega^R)$ of the path angle in the modified 3GPP dataset.

the OFDM grid is modeled to experience the same delays and doppler shifts. This results in a stationary process in the time and frequency domain, referred to as the wide-sense-stationary-uncorrelated-scattering (WSSUS) assumption (Bello, 1963). While the stationary assumptions are common in radar and wireless communications, some applications require non-stationary channel characteristics, such as the generation of long channel trajectories, that our proposed method, in its current form, cannot model.

Off-Grid Mismatches Another limitation is that our method requires a discretization of the physical parameter space (cf. Section 4.1). In consequence, when a channel in the training dataset exhibits physical parameters that do not exactly match any grid point, our proposed method cannot distinguish between having a single path with parameters between two grid points and having two paths on neighboring grid points. This mismatch is controlled by the grid resolution.

OFDM Pilot Pattern A further limitation is specific for OFDM. It is well known that compressive sensing (CS) methods experience a decrease in performance when using selection matrices that correspond to a regular pilot pattern compared to using (pseudo-)random selection matrices (Gaudio et al., 2022). As the training in SBGM builds on CS, this limitation also holds for our proposed method and constrains the set of suitable OFDM pilot patterns.

H. Modified 3GPP Dataset Description

Our modified 3GPP dataset is based on the conditionally normal channels described in (Neumann et al., 2018). More precisely, each channel realization is generated following two steps. First, we draw one random angle $\omega^{(R)}$ from the distribution illustrated in Fig. 3. Subsequently, we draw the channel \mathbf{h} from $\mathcal{N}(\mathbf{h}; \mathbf{0}, \mathbf{C}_{\omega^{(R)}})$, where

$$\mathbf{C}_{\omega^{(R)}} = \int_{-\pi}^{\pi} g(\theta; \omega^{(R)}) \mathbf{a}_R(\theta) \mathbf{a}_R(\theta)^H d\theta \quad (44)$$

and $g(\theta; \omega^{(R)})$ is a Laplacian with mean $\omega^{(R)}$ and standard deviation of 2 degree. Moreover, $\mathbf{a}_R(\cdot)|_i = e^{-j\pi(i-1)\sin(\cdot)}$ corresponding to a ULA with equidistant antenna spacing (cf. Section 4.1). The angle distribution in Fig. 3 artificially represents a scenario with, e.g., four street canyons where the users' positions are mainly distributed in four different angular regions. The 2-degree standard deviation is in line with the 3GPP standard and referred to as per-path angle spread (3GPP, 2024b). It simulates a small spread of the main angle $\omega^{(R)}$ due to scatterers close to the users. We apply no other pre-processing. We define the SNR in dB to be $\text{SNR} = 10 \log_{10}(\mathbb{E}[\|\mathbf{h}\|^2]/(\sigma^2 N))$, where N is the dimension of \mathbf{h} , i.e., the number of antennas, σ^2 is the noise variance, and $\mathbb{E}[\|\mathbf{h}\|^2]$ is estimated using 10000 samples generated in the discussed manner. For producing the training dataset, we draw SNR_i uniformly between 0dB and 20dB for each training sample and compute the corresponding noise variance σ_i^2 . Subsequently, we generate the training dataset

$$\mathcal{Y} = \{\mathbf{y}_i \mid \mathbf{y}_i = \mathbf{h}_i + \mathbf{n}_i\} \quad (45)$$

with $\mathbf{n}_i \sim \mathcal{N}_{\mathbb{C}}(\mathbf{0}, \sigma_i^2 \mathbf{I})$.

I. QuaDRiGa Dataset Description

QuaDRiGa is a freely accessible geometry-based stochastic simulation platform for wireless channels (Jaeckel et al., 2023). The QuaDRiGa dataset considered in our work builds on the “3GPP_38.901_UMa” scenario, which simulates an

Table 1. Common scenario parameters for $\mathcal{Y}_{t,f}^{(5G)}$ and $\mathcal{Y}_{t,f}^{(large)}$ in QuaDRiGa.

| Per-User Velocity Uniformly drawn from | Minimum Distance from BS | Maximum Distance from BS | Ratio of Indoor and Outdoor Users | Center Frequency | Angular Span of the BS Sector |
|---|-----------------------------|-----------------------------|--------------------------------------|---------------------|----------------------------------|
| 0-50 km/h | 20 m | 500 m | 0.3 | 6 GHz | 120 degree |

 Table 2. Specific configuration parameters for $\mathcal{Y}_{t,f}^{(5G)}$.

| Bandwidth | Subcarrier Spacing | Slot Duration | Symbol Duration |
|-----------|-----------------------|------------------|--------------------|
| 360 kHz | 15 kHz | 1 ms | 1/14 ms |

 Table 3. Specific configuration parameters for $\mathcal{Y}_{t,f}^{(large)}$.

| Bandwidth | Subcarrier Spacing | Slot Duration | Symbol Duration |
|-----------|-----------------------|------------------|--------------------|
| 1200 kHz | 60 kHz | 4.8 ms | 0.3 ms |

urban macrocell environment with parameters consistent with the 3GPP standard (Jaeckel et al., 2014). We use a mixed non-line-of-sight (NLOS)/line-of-sight (LOS) setup, where some users are in LOS with the BS and the others are not. In our simulations, we simulate channels in two different OFDM system configurations, where we denote the corresponding training datasets as $\mathcal{Y}_{t,f}^{(5G)}$ and $\mathcal{Y}_{t,f}^{(large)}$, respectively. Both datasets share common scenario parameters detailed in Table 1. The two different considered OFDM setups are characterized by their individual system configuration detailed in Table 2 and 3, respectively.

In case of $\mathcal{Y}_{t,f}^{(5G)}$ (cf. Table 2), we use a subcarrier spacing $\Delta f = 15\text{kHz}$, a symbol duration $\Delta T = \frac{1}{14}\text{ms}$ and the OFDM grid consists of 24 subcarriers and 14 time symbols in total. This results in an overall considered time (slot) duration of 1ms and an overall bandwidth of 360kHz, consistent with the 5G standard (3GPP, 2020). The overall OFDM grid contains $N = 24 \cdot 14 = 336$ resource elements.

In case of $\mathcal{Y}_{t,f}^{(large)}$ (cf. Table 3), we use a subcarrier spacing $\Delta f = 60\text{kHz}$, a symbol duration $\Delta T = 0.3\text{ms}$ and the OFDM grid consists of 20 subcarriers and 16 time symbols in total. This results in an overall considered time (slot) duration of 4.8ms and an overall bandwidth of 1200kHz. Thus, the overall OFDM grid contains $N = 20 \cdot 16 = 320$ resource elements.

In both cases, we pre-process the data before training the generative model. More specifically, we apply the common scaling of each channel realization by its effective path gain (PG), which models the attenuation due to the distance of the user and the BS as well as shadowing effects (Jaeckel et al., 2023) (i.e., the channel’s large-scale-fading). Subsequently, we scale the training dataset such that the estimated signal energy $\mathbb{E}[\|\mathbf{h}\|^2]$ equals the number of resource elements in the corresponding OFDM grid (i.e., 336 for $\mathcal{Y}_{t,f}^{(5G)}$ and 320 for $\mathcal{Y}_{t,f}^{(large)}$). For each tuple of number M of pilots and system configuration (e.g., $(30, \mathcal{Y}_{t,f}^{(5G)})$), we draw one random selection matrix as measurement matrix $\mathbf{A} \in \mathbb{R}^{M \times N}$ (cf. (5)) and keep this matrix fixed for all training and validation samples. This selection matrix extracts M random elements from the N -dimensional channel \mathbf{h} . Equivalent to the modified 3GPP dataset, we draw SNR_i uniformly between 0dB and 20dB for each training sample and compute the corresponding noise variance $\sigma_i^2 = \mathbb{E}[\|\mathbf{A}\mathbf{h}\|^2]/(M \cdot 10^{0.1\text{SNR}_i[\text{dB}]})$. Then, the datasets are given by

$$\mathcal{Y} = \{\mathbf{y}_i \mid \mathbf{y}_i = \mathbf{A}\mathbf{h}_i + \mathbf{n}_i\} \quad (46)$$

with $\mathbf{n}_i \sim \mathcal{N}_{\mathbb{C}}(\mathbf{0}, \sigma_i^2 \mathbf{I})$.

J. DeepMIMO Dataset Description

The modified 3GPP dataset (cf. Appendix H), as well as the QuaDRiGa dataset (cf. Appendix I), involve statistics in their channel generation process, due to, e.g., sampling underlying angles (modified 3GPP) or randomly placing scatterers in a simulated environment (QuaDRiGa). In addition to these channel models, we evaluate our method for SIMO based on a purely deterministic channel model, i.e., ray tracing. Next to being purely deterministic, another key difference between ray tracing and standardized channel models (and QuaDRiGa) is the absence of subpaths. More concretely, M_ℓ in (1) is set to 1 for all ℓ (Alkhateeb, 2019). Subpaths typically originate from minor effects, such as the spread of an impinging waveform at a rough surface into several paths with similar properties. Since these phenomena are difficult to simulate deterministically, they are left out in ray tracing. As described in Section 1, ray tracing requires a 3D replica of the environment of interest and the material properties within the scene. The DeepMIMO dataset proposed in (Alkhateeb, 2019) is a benchmark dataset for wireless channel modeling building on the ray tracing tool Remcom (Remcom) and offering several predefined scenarios. In

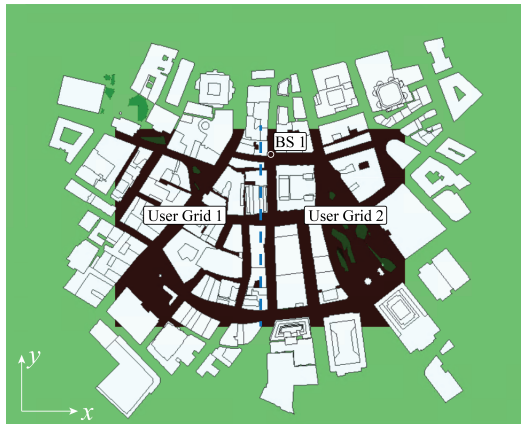


Figure 4. Ray tracing Boston scenario used in our simulation (cf. (Alkhateeb, 2019)).

our work, we use the Boston 5G scenario with 3.5GHz center frequency. In Fig. 4, we plot a 2D perspective of this scenario (Alkhateeb, 2019). We only consider users in “User Grid 2” since most of the users in “User Grid 1” are blocked and have no connection to the BS. DeepMIMO offers the possibility to simulate channels at gridpoints over the whole scenario in Fig 4, where the spacing between two adjacent users is 37cm. In a first step towards the used dataset in our work, we exclude all users in “User Grid 2”, which are blocked and have no connection to the BS, i.e., we only consider non-zero channels (either LOS or NLOS) in our dataset. Furthermore, we consider single antenna users and the BS is equipped with a ULA with N antennas and $\lambda/2$ antenna spacing. This ULA is first placed along the x-axis and then rotated by 45 degree around the z-axis. Moreover, we allow up to 8 paths to be simulated per channel realization.

We pre-process the data before training the generative models. Since the simulated channels in ray tracing involve large-scale fading (e.g., path losses due to the distance between the user and BS), their norms range over several orders of magnitude, making them ill-suited to directly train ML models. DeepMIMO provides the absolute values of each path’s path loss (denoted as `DeepMIMO_dataset{i}.user{j}.path_params.power` in DeepMIMO Version v2, and denoted as p_ℓ^{DM} in the following). Similar to how QuaDRiGa distinguishes between large-scale- and small-scale-fading (cf. (Jaeckel et al., 2023)), we scale each channel individually by $\sqrt{1/(\sum_\ell p_\ell^{\text{DM}})}$.⁸ Subsequently, we scale the training dataset such that the estimated signal energy $\mathbb{E}[\|\mathbf{h}_i\|^2]$ equals the number of antennas, i.e., N . We then apply the same method to compute noise variances σ_i^2 for each training channel realization as in Appendix H to construct the used dataset. We consider the cases $N = 8$ and $N = 32$ (and $N = 256$ for computing ground truth, cf. Appendix K), and denote the datasets as $\mathcal{Y}_{\text{DeepM}}^{(8)}$ and $\mathcal{Y}_{\text{DeepM}}^{(32)}$, respectively.

K. Architectures, Baselines, and Hyperparameters

CSVAE For the CSVAE encoder, we use a simple fully-connected NN with ReLU activation function (cf. Table 4). We tested different architectures for the decoder, from which a deep decoder-motivated architecture performed the best (cf. (Heckel & Hand, 2019)). Specifically, the decoder contains two fully connected layers with ReLU activation followed by several blocks consisting of a convolutional layer with a kernel size of 1, a ReLU activation, and a (bi-)linear upsampling operation. For the simulations on OFDM, we incorporated 3 of these blocks (cf. Table 5), while for the modified 3GPP and DeepMIMO dataset (cf. Table 6), we used 2 of them. The final layer is a convolutional layer with a kernel size of 1. We applied hyperparameter tuning for each simulation setup to adjust the width and the depth d for the encoder as well as the linear layer width and the number of convolutional channels in the decoder. For that, we took the model resulting in the largest ELBO over a validation set of 5000 samples. We used the Adam optimizer (Kingma & Ba, 2015) with a learning rate $5e-5$ for training.

⁸Note that this normalization of each individual channel requires an estimation of the attenuation of the channel based on the distance between the user and the BS, which typically changes very slowly. The alternative normalization for all channels to have norm 1, respectively, requires knowledge of each channel realization for offline training as well as online operation.

Table 4. CSVAE.

| Encoder |
|--------------------------|
| $d \times \text{Linear}$ |
| ReLU |
| $1 \times \text{Linear}$ |

Table 5. CSVAE (OFDM).

| Decoder |
|--|
| $2 \times \text{Linear}$ |
| ReLU |
| $1 \times \text{Unflatten}$ |
| $3 \times \text{Conv2D}$ (kernel size=1) |
| ReLU |
| Upsample (scale= 2, bilinear) |
| $1 \times \text{Conv2D}$ (kernel size=1) |

Table 6. CSVAE (3GPP & DeepMIMO).

| Decoder |
|--|
| $2 \times \text{Linear}$ |
| ReLU |
| $1 \times \text{Unflatten}$ |
| $2 \times \text{Conv1D}$ (kernel size=1) |
| ReLU |
| Upsample (scale=2, linear) |
| $1 \times \text{Conv1D}$ (kernel size=1) |

Table 7. Autoencoder.

| Encoder |
|--------------------------|
| $d \times \text{Conv2D}$ |
| ReLU |
| $1 \times \text{Linear}$ |
| $1 \times \text{Tanh}$ |

Table 8. Autoencoder.

| Decoder |
|--|
| $1 \times \text{Linear}$ |
| $1 \times \text{Unflatten}$ |
| $d \times \text{ConvTranspose2D}$ |
| ReLU |
| $1 \times \text{Conv2D}$ (kernel size=1) |

Table 9. GAN (OFDM).

| Generator |
|--|
| $1 \times \text{Linear}$ |
| ReLU |
| $1 \times \text{Unflatten}$ |
| $2 \times \text{Upsample}$ (scale=2,nearest) |
| Conv2D |
| Batch Normalization |
| ReLU |
| $1 \times \text{Conv2D}$ |

Table 10. GAN (OFDM).

| Discriminator |
|---------------------------|
| $3 \times \text{Conv2D}$ |
| LeakyReLU(0.2) |
| Dropout($p = 0.25$) |
| $1 \times \text{Flatten}$ |
| $1 \times \text{Linear}$ |

CSGMM The only hyperparameter for CSGMM is the number K of components. We tune this parameter by choosing K , leading to the largest log-likelihood over the training dataset.

Autoencoder We use an autoencoder to apply the cross-validation method from (Baur et al., 2024c; Xiao et al., 2022). The chosen architecture resembles the proposed architecture in (Rizzello & Utschick, 2021) and is given in Table 7 and 8. The kernel size, the stride, and the padding of the 2D convolutional layers in the encoder are set to 3, 2, and 1, respectively. The stride and the padding in the 2D transposed convolutional layers of the decoder are set to 2 and 1, and the kernel size is set to either 3 or 4 depending on the output dimension to be matched. The final 2D convolutional layer has a kernel size, stride, and padding of 1, 1, and 0. We used the same architecture for the simulations on DeepMIMO but with 1D convolutional layers instead of 2D ones. All autoencoders in all simulations exhibit a latent dimension of 16. We applied hyperparameter tuning to adjust the width of the linear layer, the number of convolutional blocks d as well as the channel size of the convolutional layers based on a ground-truth validation dataset. For QuaDRiGa, we used 10000 validation channel realizations. For DeepMIMO, we used 50000 validation channel realizations. We used the Adam optimizer (Kingma & Ba, 2015) with a learning rate $5e-5$ for training.

AmbientGAN and GAN-rbf For both GAN variants, the AmbientGAN and the GAN-rbf, we utilize the architecture from (Doshi et al., 2022), i.e., the generator consists of a single fully connected layer with ReLU activation, an unflatten operation and, subsequently, two blocks of a nearest-neighbor upsampling operation, a convolutional layer, a batch normalization and a ReLU activation (cf. Table 9). The final layer is a convolutional layer. The kernel size, the stride, and the padding of all convolutional layers are set to 3, 1, and 1, respectively. The discriminator contains three blocks of a convolutional layer, a LeakyReLU activation, and a dropout layer. Subsequently, it contains a flatten operation and a final linear layer. For the simulations on DeepMIMO, we use the same architecture but with 1D convolutional layers instead of 2D ones. The width of the linear layers and the channel number of the convolutional layers is determined by hyperparameter tuning. We take the reconstruction performance in channel estimation as the objective for the hyperparameter tuning. More precisely, we reconstruct channels from validation samples using the GAN and take the model resulting in the smallest average measurement error (Bora et al., 2018). In line with (Doshi et al., 2022), we used the RMSProp optimizer with a learning rate $5e-5$ for training, and the GAN variants are optimized using the Wasserstein GAN objective with gradient penalty.

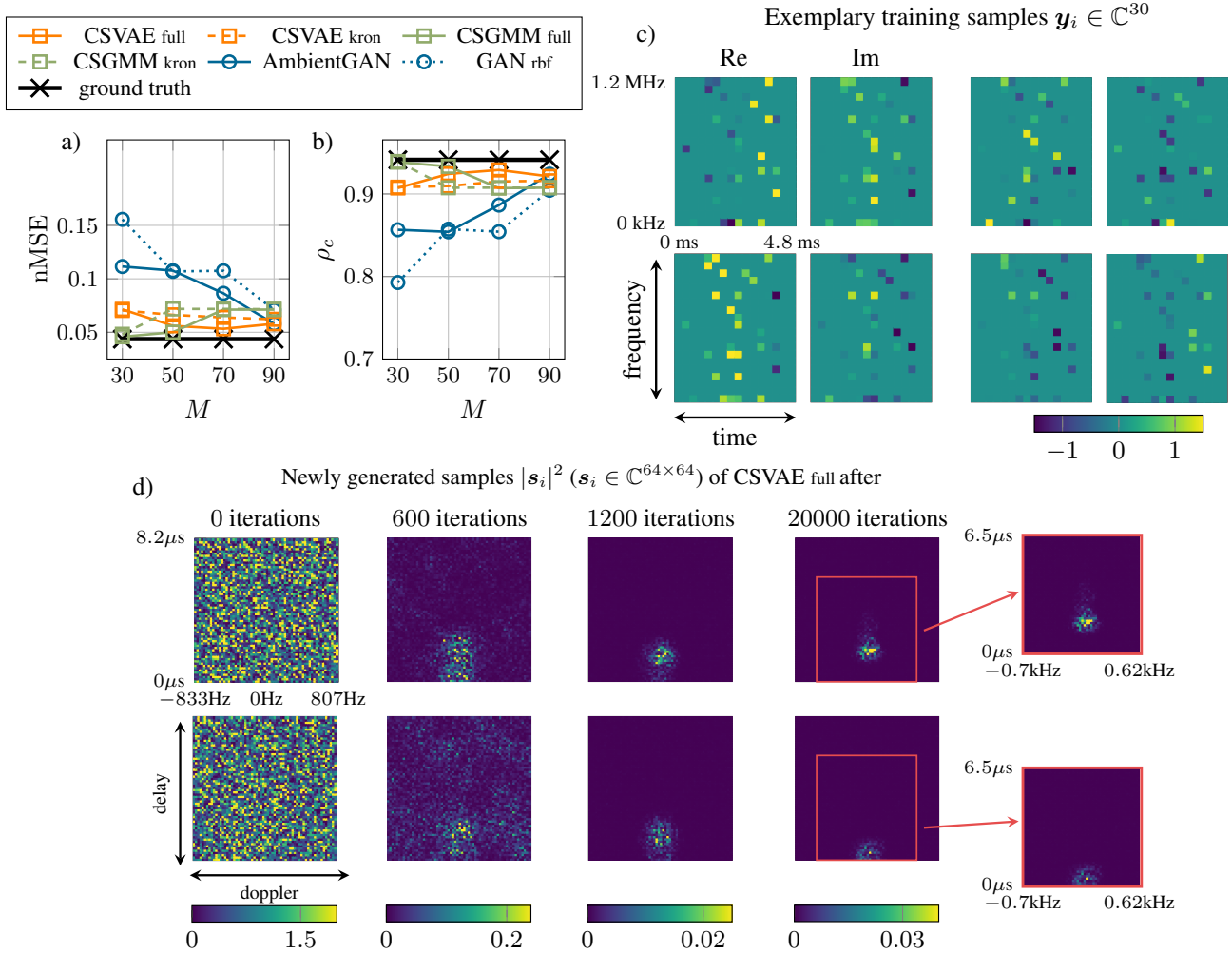


Figure 5. a) and b) nMSE and ρ_c for reconstructing ground-truth channels by an autoencoder trained on channel realizations produced by the generative models, respectively. We vary the number M of pilot symbols with fixed $N_t = 10000$, c) four exemplary training samples, d) illustration of the CSVAE full training by plotting the squared absolute value of two generated samples after 0, 600, 1200, and 20000 iterations during training.

Ground-Truth Baseline for the Parameter Generation Performance In Section 6.2, we evaluate the parameter generation performance for the 3GPP dataset and compare our method to ground-truth. The same is done for the DeepMIMO dataset in Appendix 6.2. In general, for the simulation, we decide on a number of angle grid points S , set to 256. For computing the results for the ground-truth baseline, we artificially assume that we have as many antennas as gridpoints, i.e., 256. This results in \mathbf{D}_R in (6) to be squared and invertible. In consequence, we can compute \mathbf{s}_R for each channel realization in the test set and estimate the power angular profile (13) and the angular spread (14) using these calculated vectors.

L. Additional Results

OFDM with 1.2MHz Bandwidth and 4.8ms Overall Duration In Fig. 2, we analyze the training as well as the channel generation performance of our proposed model on 5G-consistent OFDM grids, i.e., having 24 subcarriers with 15kHz subcarrier spacing and 14 time symbols with an overall duration of 1ms. However, larger bandwidths and longer time durations generally allow the corresponding delay-doppler domain (i.e., the resulting domain by applying the FT in the time-frequency domain) to be represented with a higher resolution. Therefore, we analyze a further OFDM system configuration with a bandwidth of 1.2MHz and 4.8ms overall duration. The subcarrier spacing is set to 60kHz and the symbol duration to 0.3ms. The dataset is denoted by $\mathcal{Y}_{t,f}^{(\text{large})}$ (cf. Appendix I for more details). In Fig. 5 a) and b), the

Table 11. Generalization Performance for OFDM ($M = 30$, $N_t = 10000$).

| | CSVAE full trained on $\mathcal{Y}_{t,f}^{(5G)}$ | CSVAE full trained on $\mathcal{Y}_{t,f}^{(large)}$ |
|---------------------------------------|---|--|
| nMSE for the OFDM (5G) config. | 0.0031 | <u>0.0032</u> |
| nMSE for the OFDM (large) config. | <u>0.0725</u> | 0.0714 |
| ρ_c for the OFDM (5G) config. | 0.9945 | <u>0.9944</u> |
| ρ_c for the OFDM (large) config. | <u>0.9063</u> | 0.9073 |

nMSE and ρ_c of the autoencoder reconstruction are shown over the number M of pilot symbols with fixed $N_t = 10000$. We plot the performance of our proposed method without (full) and with (kron) Kronecker approximation (cf. Section 4.4). We choose $S_t = S_f = 64$. Moreover, $\bar{\tau} = 8.2\mu\text{s}$ and $\bar{\nu} = 1.64\text{kHz}$ (cf. Section 4.1). For $M \leq 70$, our proposed methods all outperform the baselines AmbientGAN and GAN-rbf. For $M = 90$, all models perform approximately the same. It is noteworthy that CSGMM full and kron perform worse for larger M . We observed that for large M and $\mathcal{Y}_{t,f}^{(large)}$, the training of CSGMM tends to collapse in the sense that effectively only one component contributes to the CSGMM. One possible explanation is that for larger M , the log-evidence that is optimized (as a function of $\{\rho_k, \gamma_k\}_{k=1}^K$) is parameterized by higher dimensional observations \mathbf{y}_i . Thus, although having access to more information in theory, it is possible to end up in a worse local optimum compared to having a simpler objective with a smaller M . In Fig. 5 c), four exemplary training samples are shown. Equivalent to Fig. 2, we plot the 30-dimensional observations within the corresponding OFDM grid representing the dimensions of the underlying channel $\mathbf{H} \in \mathbb{C}^{20 \times 16}$ with $\mathbf{h} = \text{vec}(\mathbf{H}) \in \mathbb{C}^{320}$. Moreover, we also plot the squared absolute value of two samples in the delay-doppler domain during training in Fig. 5 d).

Generalizability for OFDM We analyze our proposed method’s capability to generalize to other system configurations without being retrained. More specifically, we train CSVAE full using $\mathcal{Y}_{t,f}^{(5G)}$, $M = 30$ and $N_t = 10000$. After training, we use the dictionary $\mathbf{D}_{t,f}$ for the OFDM (large) configuration, i.e., $\Delta f = 60\text{kHz}$, $\Delta T = 0.3\text{ms}$ with $\mathbf{D}_{t,f} \in \mathbb{C}^{(20 \cdot 16) \times (64 \cdot 64)}$ (cf. Appendix A) to map generated $\mathbf{s}_{t,f}$ to new channel realizations that are different to the ones involved in the training dataset $\mathcal{Y}_{t,f}^{(5G)}$. Subsequently, we apply the same cross-validation method as in Fig. 2, i.e., we use these newly generated channel realizations to train an autoencoder whose performance is then evaluated on ground-truth QuaDRiGa channels in the OFDM (large) configuration. We also do the same procedure vice versa, i.e., we train CSVAE full using $\mathcal{Y}_{t,f}^{(large)}$, $M = 30$ and $N_t = 10000$, and then adapt the dictionary to the OFDM (5G) configuration. The results are given in Table 11. The underlined numbers indicate the performance where CSVAE full has been trained on a different system configuration compared to the one used for channel generation. We can see that there is almost no difference between whether CSVAE full has been trained on the system configuration that matches with the generated channel realizations afterward or a different one.

Controlling the Number of Paths per Generated Channel Realization When modeling wireless channels using ray tracing, one possibility is to customize the number of paths per channel realization (Alkhateeb, 2019). This can be beneficial to, e.g., reduce computational complexity or only capture the most relevant effects in the channel realization of interest. Equivalent to ray tracing, our proposed method also allows the adjustment of the number of paths. More precisely, our method generates new complex-valued vectors $\mathbf{s}_{t,f}$ (or \mathbf{s}_R) where each entry represents the complex-valued path loss corresponding to one gridpoint, i.e., one delay-doppler tuple or one angle. Thus, we can interpret each non-zero entry in $\mathbf{s}_{t,f}$ as a single path, where the corresponding index in $\mathbf{s}_{t,f}$ together with the complex-valued entry determines the path’s physical parameters. Thus, when we want to restrict our generated channel realizations to only possess p_{\max} paths, we can set all entries in the newly generated $\mathbf{s}_{t,f}$ (or \mathbf{s}_R) to zero that do not belong to the p_{\max} strongest entries in a squared absolute value sense.

In Fig. 6, we analyze the effect on the generated samples when varying p_{\max} . More precisely, in Fig. 6 a) and b), the nMSE and ρ_c are shown for varying p_{\max} where we used QuaDRiGa channels from the OFDM (large) configuration (cf. Section I), $M = 30$ and $N_t = 10000$. Thus, we first train CSVAE full with $\mathcal{Y}_{t,f}^{(large)}$. We then generate 10000 new samples $\mathbf{s}_{t,f}$. We filter out all entries for each of these samples with a smaller squared absolute value than the p_{\max} strongest entries. We then map the resulting vectors to channel realizations using the dictionary $\mathbf{D}_{t,f}$ and train the autoencoder. We see that by

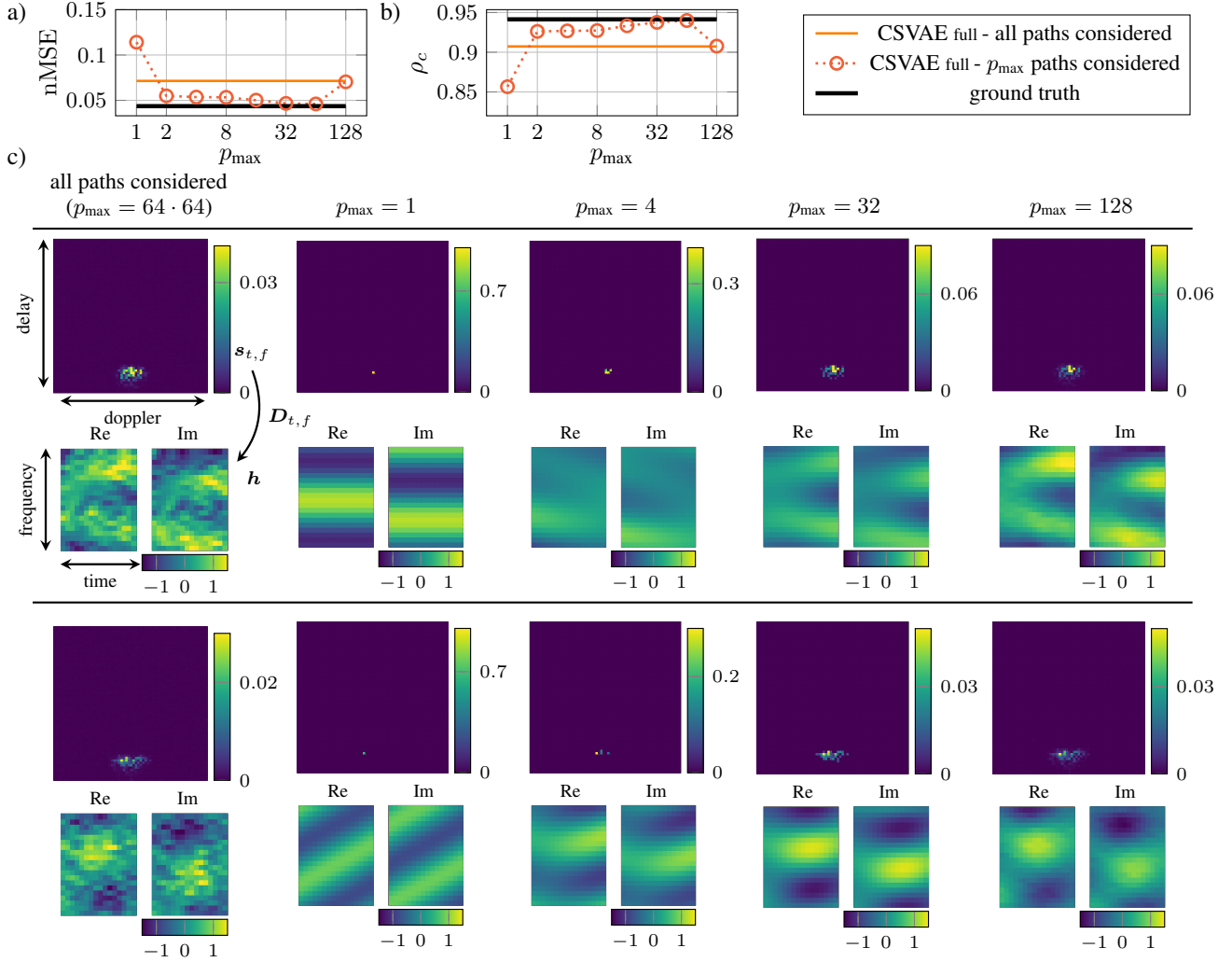


Figure 6. a) and b) nMSE and ρ_c over the number of considered paths p_{\max} for the OFDM (large) configuration (cf. Appendix I), $M = 30$ and $N_t = 10000$, c) illustration of two newly generated samples $s_{t,f}$ (first and third row) and their corresponding channel realizations h after applying the dictionary $D_{t,f}$ (second and fourth row) for varying p_{\max} (from left to right).

incorporating the prior knowledge that most channels only exhibit a few relevant paths, we improve our method even further and reach the ground-truth performance.

Thus, p_{\max} operates as a regularization that neutralizes granular noise within the generated samples in the delay-doppler domain stemming from non-perfect training. In Fig 6 c), we illustrate the effect of p_{\max} for two exemplary generated samples. We can see that when we do not filter out any entries in $s_{t,f}$, the resulting channel realizations exhibit non-smooth characteristics in the time-frequency domain, whereas when incorporating p_{\max} , smoother channel realizations are produced. However, this perceptual reasoning is limited as we see that the reconstruction performance is the same for considering no p_{\max} compared to setting p_{\max} to 128, while perceptually, $p_{\max} = 128$ leads to smoother channel realizations.

Pseudocode for generating channel realizations with a restricted number of paths is given in Appendix M.

DeepMIMO Results For the DeepMIMO dataset on SIMO, we evaluate the parameter as well as the channel generation performance. Equivalent to the results on the modified 3GPP dataset in Fig. 1, we plot four exemplary training samples in Fig. 7 a), the absolute squared value for three exemplary newly generated samples of CSVAE, CSGMM compared to ground-truth in Fig. 7 b), and the power angular profile and a histogram of the angular spread in Fig. 7 c). The results are in line with the results on the modified 3GPP dataset with CSGMM exhibiting less peaks and matches the underlying power angular profile more closely. In addition, CSVAE underestimates the amount of LOS channels, which can be seen at the missing peak in the histogram with very small angular spreads.

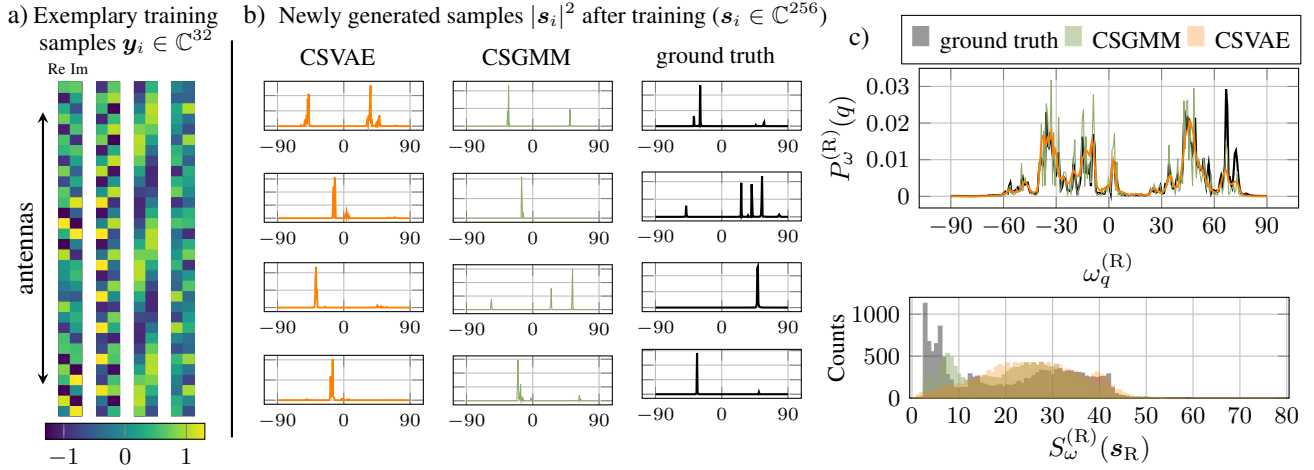


Figure 7. a) Four exemplary training samples, b) squared absolute value of four exemplary generated samples of CSVAE, CSGMM and ground truth, respectively, c) power angular profile $P_\omega^{(R)}(q)$ and a histogram of the angular spread $S_\omega^{(R)}(\mathbf{s}_R)$ from 10000 generated samples by the CSVAE and CSGMM compared to ground truth.

Table 12. Channel Realization Performance for DeepMIMO SIMO ($M = N = 32$, $S = 256$, $N_t = 10000$).

| | CSVAE no p_{\max} | CSVAE $p_{\max} = 8$ | CSGMM no p_{\max} | CSGMM $p_{\max} = 8$ | AmbientGAN | ground-truth |
|----------|------------------------|-------------------------|------------------------|-------------------------|------------|--------------|
| nMSE | 0.037 | 0.038 | 0.035 | 0.037 | 0.054 | 0.027 |
| ρ_c | 0.957 | 0.957 | 0.959 | 0.957 | 0.938 | 0.970 |

Table 13. Generalization Performance for DeepMIMO SIMO ($S = 256$, $N_t = 10000$).

| | CSVAE trained on $\mathcal{Y}_{\text{DeepM}}^{(32)}$ | CSGMM trained on $\mathcal{Y}_{\text{DeepM}}^{(32)}$ | CSVAE trained on $\mathcal{Y}_{\text{DeepM}}^{(8)}$ | CSGMM trained on $\mathcal{Y}_{\text{DeepM}}^{(8)}$ |
|--------------------------------|---|---|--|--|
| nMSE for $N = 32$ antennas | 0.037 | 0.035 | <u>0.043</u> | <u>0.042</u> |
| ρ_c for $N = 32$ antennas | 0.957 | 0.959 | <u>0.948</u> | <u>0.950</u> |

In Table 12, the channel generation performance is evaluated. More precisely, we train the generative models using $N_t = 10000$ noisy channel observations and generate $N_{\text{gen}} = 50000$ channel realizations afterward. These channels are then used to train an autoencoder whose performance is shown in Table 12. As there is no measurement matrix masking out entries in \mathbf{h} , GAN-rbf cannot be used as a baseline, so we only compare to AmbientGAN. It can be seen that all our proposed models outperform the baseline. Moreover, constraining the number of paths and setting p_{\max} to 8 did not improve the performance.

In Table 13, we evaluate the generalizability of our proposed methods on the DeepMIMO dataset. Specifically, we train our proposed method with $\mathcal{Y}_{\text{DeepM}}^{(8)}$ (cf. Appendix J), i.e., we utilize $N = 8$ antennas. After training, we exchange the dictionary with a dictionary whose range covers $N = 32$ antennas. We then generate 50000 channel realizations and train the autoencoder as previously described. The autoencoder's performance is given in Table 13. It can be seen that there is only a minor decrease in performance when using $N = 8$ antennas during training and then generating channels corresponding to $N = 32$ antennas compared to having 32-dimensional channels already during training.

M. Pseudocode for the Parameter and Channel Generation

Algorithms 1-3 summarize the generation process of parameters, channels, and channels with constraining the path number, respectively.

Algorithm 1 Parameter Generation with the CSGMM (CSVAE)

Input: –

Output: complex-valued vectors $\{\mathbf{s}_i\}_{i=1}^{N_{\text{gen}}}$ whose entries together with their indices correspond to the physical parameters (depending on the grid used for training)

for $i = 1$ **to** $N_{(\text{gen})}$ **do**

1) draw $k_i \sim p(k)$ (or draw $\mathbf{z}_i \sim p(\mathbf{z})$) (cf. Section 4.4)

2) draw $\mathbf{s}_i \sim p(\mathbf{s}|k_i) = \mathcal{N}_{\mathbb{C}}(\mathbf{s}; \mathbf{0}, \text{diag}(\gamma_i))$ (or draw $\mathbf{s}_i \sim p(\mathbf{s}|\mathbf{z}_i) = \mathcal{N}_{\mathbb{C}}(\mathbf{s}; \mathbf{0}, \text{diag}(\gamma_{\theta}(\mathbf{z}_i)))$) (cf. Section 4.4)

end for

Algorithm 2 Channel Generation with the CSGMM (CSVAE)

Input: dictionary $\mathbf{D}^{(\text{new})}$ that can be chosen according to the desired system configuration of interest (not necessarily the one used for training)

Output: complex-valued channel realizations $\{\mathbf{h}_i\}_{i=1}^{N_{\text{gen}}}$ that are scenario-specific and match the desired system configuration of interest

for $i = 1$ **to** $N_{(\text{gen})}$ **do**

1) draw $k_i \sim p(k)$ (or draw $\mathbf{z}_i \sim p(\mathbf{z})$) (cf. Section 4.4)

2) draw $\mathbf{s}_i \sim p(\mathbf{s}|k_i) = \mathcal{N}_{\mathbb{C}}(\mathbf{s}; \mathbf{0}, \text{diag}(\gamma_i))$ (or draw $\mathbf{s}_i \sim p(\mathbf{s}|\mathbf{z}_i) = \mathcal{N}_{\mathbb{C}}(\mathbf{s}; \mathbf{0}, \text{diag}(\gamma_{\theta}(\mathbf{z}_i)))$) (cf. Section 4.4)

3) compute $\mathbf{h}_i = \mathbf{D}^{(\text{new})} \mathbf{s}_i$

end for

Algorithm 3 Channel Generation with the CSGMM (CSVAE) when only considering p_{max} paths

Input: dictionary $\mathbf{D}^{(\text{new})}$ that can be chosen according to the desired system configuration of interest (not necessarily the one used for training)

Output: complex-valued channel realizations $\{\mathbf{h}_i\}_{i=1}^{N_{\text{gen}}}$ that are scenario-specific and match the desired system configuration of interest

for $i = 1$ **to** $N_{(\text{gen})}$ **do**

1) draw $k_i \sim p(k)$ (or draw $\mathbf{z}_i \sim p(\mathbf{z})$) (cf. Section 4.4)

2) draw $\mathbf{s}_i \sim p(\mathbf{s}|k_i) = \mathcal{N}_{\mathbb{C}}(\mathbf{s}; \mathbf{0}, \text{diag}(\gamma_i))$ (or draw $\mathbf{s}_i \sim p(\mathbf{s}|\mathbf{z}_i) = \mathcal{N}_{\mathbb{C}}(\mathbf{s}; \mathbf{0}, \text{diag}(\gamma_{\theta}(\mathbf{z}_i)))$) (cf. Section 4.4)

3) compute $|\mathbf{s}_i|^2$ and identify the indices \mathcal{I}_i of the p_{max} strongest entries in $|\mathbf{s}_i|^2$

4) compute $\tilde{\mathbf{s}}_i$ which equals \mathbf{s}_i for the indices in \mathcal{I}_i and is zero elsewhere

3) compute $\mathbf{h}_i = \mathbf{D}^{(\text{new})} \tilde{\mathbf{s}}_i$

end for
